

Turbulence in the two-dimensional Fourier-truncated Gross-Pitaevskii equation

Vishwanath Shukla¹, Marc Brachet² and Rahul Pandit¹ ‡

¹ Centre for Condensed Matter Theory, Department of Physics, Indian Institute of Science, Bangalore 560012, India

² Laboratoire de Physique Statistique de l'Ecole Normale Supérieure, associé au CNRS et aux Universités Paris VI et VII, 24 Rue Lhomond, 75231 Paris, France

E-mail: vishwanath@physics.iisc.ernet.in, brachet@physique.ens.fr, rahul@physics.iisc.ernet.in

Abstract. We undertake a systematic, direct numerical simulation (DNS) of the two-dimensional, Fourier-truncated, Gross-Pitaevskii equation to study the turbulent evolutions of its solutions for a variety of initial conditions and a wide range of parameters. We find that the time evolution of this system can be classified into four regimes with qualitatively different statistical properties. First, there are transients that depend on the initial conditions. In the second regime, power-law scaling regions, in the energy and the occupation-number spectra, appear and start to develop; the exponents of these power-laws and the extents of the scaling regions change with time and depended on the initial condition. In the third regime, the spectra drop rapidly for modes with wave numbers $k > k_c$ and partial thermalization takes place for modes with $k < k_c$; the self-truncation wave-number $k_c(t)$ depends on the initial conditions and it grows either as a power of t or as $\log t$. Finally, in the fourth regime, complete-thermalization is achieved and, if we account for finite-size effects carefully, correlation functions and spectra are consistent with their nontrivial Berezinskii-Kosterlitz-Thouless forms.

PACS numbers: 47.27.Ak, 47.27.Gs, 47.37.+q, 67.25.dk, 67.25.dj

1. Introduction

The elucidation of the nature of superfluid turbulence, which began with the pioneering studies of Feynman [1] and of Vinen and Hall [2–6], has continued to engage the attention of experimentalists, theoreticians, and numerical simulators [7–13]. Experimental systems, in which such turbulence is studied, include the bosonic superfluid ^4He , its fermionic counterpart ^3He , and Bose-Einstein condensates (BECs) of cold atoms in traps and their optical analogues; for representative studies we refer the reader to [14–23]. Theoretical and numerical studies have used a variety of models to

‡ Also at Jawaharlal Nehru Centre For Advanced Scientific Research, Jakkur, Bangalore, India

study superfluid turbulence; these include the two-fluid model [24, 25], Biot-Savart-type models with [26, 27] or without [28, 29] the local-induction approximation, and the Gross-Pitaevskii (GP) or nonlinear Schrödinger (NLS) equations [30, 31]. These models have been studied by a combination of theoretical methods, such as wave-turbulence theory [30–33], and numerical simulations [34–40]. Most of these studies have been carried out in three dimensions (3D); numerical simulations of two-dimensional (2D) models for superfluid turbulence have been increasing steadily over the past few years [41–44]. Here we undertake a systematic direct numerical simulation (DNS) of the dissipationless, unforced, Fourier-truncated, 2D, GP equation with a view to identifying what, if any, features of the turbulent evolution of the solutions of this equation are universal, i.e., they do not depend on initial conditions. Some, though not all, parts of our results are contained in earlier simulations [41–47]. The perspective of our study is different from earlier studies of the 2D GP equation; in particular, we elucidate in detail the dynamical evolution of this system and examine the various stages of its thermalization; in this sense our work is akin to recent studies of thermalization in Euler and other hydrodynamical equations [48–50]; a similar study for the 3D GP equation has been carried out by Krstulovic and Brachet [38, 51].

It is useful to begin with a qualitative overview of our principal results. We find that the dynamical evolution of the dissipationless, unforced, 2D, Fourier-truncated GP equation can be classified, roughly, into the following four regimes, which have qualitatively different statistical properties: (1) The first is the region of initial transients; this depends on the initial conditions. (2) This is followed by the second regime, in which we see the onset of thermalization; here the energy and occupation-number spectra begin to show power-law-scaling behaviours, but the power-law exponent and the extents of the scaling regions change with time and depend on the initial conditions. (3) In the third regime, which we call the region of partial thermalization, these spectra show clear, power-law, scaling behaviours, with a power that is independent of the initial conditions, and, at large wave vectors, an initial-condition-dependent, self-truncation regime, where spectra drop rapidly; (4) finally, in the fourth regime, the system thermalizes completely and exhibits correlation functions that are consistent with the predictions of the Berezinskii-Kosterlitz-Thouless (BKT) theory [47, 52–54], if the simulation domain and simulation time are large enough. Although some of these regimes have been seen in some earlier numerical studies of the 2D GP equation, we are not aware of any study that has systematized the study of these four dynamical regimes. In particular, regime 3, which shows partial thermalization and self-truncation in spectra, has not been identified in the 2D, Fourier-truncated, GP equation, even though its analogue has been investigated in the 3D case [32, 38, 51].

The remaining part of this paper is organised as follows. In section 2, we describe the 2D, GP equation and the different statistical measures we use to characterize turbulence in the Fourier-truncated, 2D, GP equation (section 2.1); the details of our numerical methods and initial conditions are given in section 2.2. In section 3, we present our results; these are described in the four subsections 3.1–3.4 that are devoted,

respectively, to the following: (a) the temporal evolution of the energy components, velocity-component probability distribution functions (PDFs), and the population N_0 in the zero-wave-number mode; (b) the statistical characterization of the first two regimes of the dynamical evolution (by using various energy and the occupation-number spectra for different initial conditions); (c) a similar statistical characterization, as in subsection 3.2, but for the regime with partial thermalization, and the study of the nature of the growth of the self-truncation region; (d) the final, completely thermalized state of the Fourier-truncated, 2D, GP equation. Section 4 contains our conclusions. A note on the units used for the GP equation and the details of some analytical calculations are presented in Appendix A and Appendix B, respectively.

2. Model, Initial Conditions, and Numerical Methods

In this Section, we describe the 2D, GP equation. We define all the statistical measures that we use to characterize the time evolution of this equation, given the three types of initial conditions that we describe below. We also describe the numerical methods, and computational procedures that we use to solve this equation.

2.1. The Gross-Pitaevskii Equation

The GP equation, which describes the dynamical evolution of the wave function ψ of a weakly interacting 2D Bose gas at low temperatures, is

$$i\frac{\partial\psi(\mathbf{x}, t)}{\partial t} = -\nabla^2\psi(\mathbf{x}, t) + g|\psi|^2\psi(\mathbf{x}, t); \quad (1)$$

$\psi(\mathbf{x}, t)$ is a complex, classical field and g is the effective interaction strength [55, 56]. This equation conserves the total energy

$$E = \int_{\mathcal{A}} \left[|\nabla\psi|^2 + \frac{1}{2}g|\psi|^4 \right] d^2x \quad (2)$$

and the total number of particles

$$N = \int_{\mathcal{A}} |\psi|^2 d^2x, \quad (3)$$

where $\mathcal{A} = L^2$ is the area of our 2D, periodic, computational domain of side L . From (1) we obtain the continuity equation

$$\frac{\partial\rho}{\partial t} + \nabla \cdot (\rho\mathbf{v}) = 0, \quad (4)$$

where $\rho = |\psi|^2$ is interpreted as the particle density and the velocity is

$$\mathbf{v}(\mathbf{x}, t) = \frac{\psi^*\nabla\psi - \psi\nabla\psi^*}{i|\psi|^2}. \quad (5)$$

We can use the Madelung transformation $\psi(\mathbf{x}, t) = \sqrt{\rho}e^{i\theta(\mathbf{x}, t)}$, where $\theta(\mathbf{x}, t)$ is the phase of $\psi(\mathbf{x}, t)$, to write $\mathbf{v}(\mathbf{x}, t) = 2\nabla\theta(\mathbf{x}, t)$, whence we get [35]

$$E = \int_{\mathcal{A}} \left[\frac{1}{4}\rho v^2 + \frac{1}{2}g|\psi|^4 + [\nabla\rho^{1/2}]^2 \right] d^2x = E_{kin} + E_{int} + E_q, \quad (6)$$

where the kinetic, interaction, and quantum-pressure energies are defined, respectively, as

$$E_{kin} = \frac{1}{4} \int_{\mathcal{A}} |\sqrt{\rho}v|^2 d^2x, \quad (7a)$$

$$E_{int} = \frac{1}{2} \int_{\mathcal{A}} g|\psi|^4 d^2x, \quad (7b)$$

$$E_q = \int_{\mathcal{A}} \nabla|\rho^{1/2}|^2 d^2x. \quad (7c)$$

We separate the compressible (superscript c) and the incompressible (superscript i) parts of the kinetic energy by making use of the decomposition

$$\rho^{1/2}\mathbf{v} = (\rho^{1/2}\mathbf{v})^i + (\rho^{1/2}\mathbf{v})^c, \quad (8)$$

where $\nabla \cdot (\rho^{1/2}\mathbf{v})^i = 0$ and $\nabla \times (\rho^{1/2}\mathbf{v})^c = 0$, whence we obtain the following:

$$E_{kin}^i = \frac{1}{4} \int_{\mathcal{A}} |(\sqrt{\rho}v)^i|^2 d^2x; \quad (9a)$$

$$E_{kin}^c = \frac{1}{4} \int_{\mathcal{A}} |(\sqrt{\rho}v)^c|^2 d^2x. \quad (9b)$$

The spectra for these energies are defined as follows:

$$E_{kin}^i = \frac{1}{4} \int |\widehat{(\rho^{1/2}\mathbf{v})^i}|^2 d^2k \equiv \int E_{kin}^i(k) dk; \quad (10)$$

$$E_{kin}^c = \frac{1}{4} \int |\widehat{(\rho^{1/2}\mathbf{v})^c}|^2 d^2k \equiv \int E_{kin}^c(k) dk; \quad (11)$$

$$E_{int} = \int |\sqrt{g/2}|\widehat{\psi}|^2|^2 d^2k \equiv \int E_{int}(k) dk; \quad (12)$$

and

$$E_q = \int |\widehat{\nabla\rho^{1/2}}|^2 d^2k \equiv \int E_q(k) dk; \quad (13)$$

furthermore, we define an occupation-number spectrum $n(k)$ via

$$N = \int |\widehat{\psi}|^2 d^2k \equiv \int n(k) dk; \quad (14)$$

here we denote the Fourier transform of $A(\mathbf{x})$ by \widehat{A} ; and, for notational convenience, we do not show explicitly the dependence of these spectra on time t . In any computational study, we must limit the number of Fourier modes that we use in our study of the GP

equation; we refer to such a GP equation as a Fourier-truncated GP equation (cf. [48,49] for studies of the Fourier- or Galerkin-truncated Euler equation).

The Bogoluibov dispersion relation $\omega_B(k)$ is obtained by linearizing (1) around a constant ψ . For a total number of particles (3) $N = 1$, it is

$$\omega_B(k) = kc\sqrt{1 + \frac{\xi^2 k^2}{2}}, \quad (15)$$

where the sound velocity is $c = \frac{\sqrt{2g}}{L}$ and the coherence length is

$$\xi = \frac{L}{\sqrt{g}}. \quad (16)$$

We investigate thermalization in the 2D GP equation, so it is useful to recall that a uniform, interacting, 2D Bose gas has a high-temperature disordered phase and a low-temperature, Berezenskii-Kosterlitz-Thouless (BKT) phase [57–60], which shows quasi-long-range order with an algebraic decay of the spatial correlation function [52]

$$c(r) = \langle [e^{-i\theta(\mathbf{x})} - \langle e^{-i\theta(\mathbf{x})} \rangle] [e^{i\theta(\mathbf{x}+\mathbf{r})} - \langle e^{i\theta(\mathbf{x}+\mathbf{r})} \rangle] \rangle; \quad (17)$$

for temperatures T below the transition temperature T_{BKT} (or energy E_{BKT} in the microcanonical ensemble),

$$c(r) \sim r^{-\eta}, \quad (18)$$

where $r \equiv |\mathbf{r}|$ and the critical exponent $\eta < 0.25$ for $T < T_{BKT}$; and $\eta = 0.25$ at $T = T_{BKT}$ [53]. The BKT phase shows bound vortex-antivortex pairs; these unbind above T_{BKT} , so

$$c(r) \sim e^{-r/\ell}, \quad (19)$$

in the disordered phase, with ℓ the correlation length.

2.2. Numerical Methods and Initial Conditions

To perform a systematic, pseudospectral, direct numerical simulation (DNS) of the spatiotemporal evolution of the 2D, Fourier-truncated, GP equation, we have developed a parallel, MPI code in which we discretize $\psi(\mathbf{x}, t)$ on a square simulation domain of side $L = 32$ with N_c^2 collocation points. We use periodic boundary conditions in both spatial directions, because we study homogeneous, isotropic turbulence in this 2D system, and a fourth-order, Runge-Kutta scheme, with time step Δt , for time marching. We evaluate the linear term in (1) in Fourier space and the nonlinear term in physical space; for the Fourier-transform operations we use the FFTW library [61]. Thus, the maximum wave number $k_{max} = (N_c/2)\Delta k$, where $\Delta k = 2\pi/L$, and

$$\xi k_{max} = \frac{\pi N_c}{\sqrt{g}}. \quad (20)$$

We have checked that, for the quantities we calculate, dealiasing of our pseudospectral code does not change our results substantially; here we present the results from our pseudospectral simulations that do not use dealiasing.

To initiate turbulence in the 2D GP equation we use three types of initial conditions IC1 [41], IC2, and IC3 [51], always normalized to correspond to a total number of particles (3) $N = 1$. The first of these is best represented in Fourier space as follows:

$$\widehat{\psi}(\mathbf{k}, t = 0) = \frac{1}{\sqrt{\pi^{1/2}\sigma}} \exp\left(-\frac{(k - k_0)^2}{2\sigma^2}\right) \exp(i\Theta(k_x, k_y)), \quad (21)$$

where $k = \sqrt{k_x^2 + k_y^2}$, $\Theta(k_x, k_y)$ are random numbers distributed uniformly on the interval $[0, 2\pi]$; $k_0 = \mathcal{N}_0\Delta k$ and $\sigma = \mathcal{B}\Delta k$, where the integer \mathcal{N}_0 controls the spatial scale at which energy is injected into the system, and the real number \mathcal{B} specifies the Fourier-space width of $\widehat{\psi}$ at time $t = 0$. The initial condition IC2 is like IC1 but, in addition, it has a finite initial condensate population $N_0^i = |\widehat{\psi}(\mathbf{k} = 0, t)|^2 (\Delta k)^2$ at time $t = 0$.

We obtain the initial condition IC3 by solving the 2D, stochastic, Ginzburg-Landau equation (SGLE), which follows from the free-energy functional

$$\mathcal{F} = \int_{\mathcal{A}} d^2x \left(|\nabla\psi|^2 - \mu|\psi|^2 + \frac{1}{2}g|\psi|^4 \right), \quad (22)$$

where μ is the chemical potential§. The SGLE is

$$\frac{\partial\psi}{\partial t} = -\frac{\delta\mathcal{F}}{\delta\psi^*} + \zeta(\mathbf{x}, t), \quad (23)$$

where ζ is a zero-mean, Gaussian white noise with

$$\langle \zeta(\mathbf{x}, t)\zeta^*(\mathbf{x}', t') \rangle = D\delta(\mathbf{x} - \mathbf{x}')\delta(t - t'), \quad (24)$$

where $D = 2T$, in accordance with the fluctuation-dissipation theorem [62], T is the temperature, and δ the Dirac delta function. Finally, the SGLE (23) becomes

$$\frac{\partial\psi}{\partial t} = \nabla^2\psi - \mu\psi + g|\psi|^2\psi + \zeta, \quad (25)$$

which we solve along with the following, ad-hoc equation

$$\frac{d\mu}{dt} = -\frac{\nu_N}{\mathcal{A}}(N - N_{\text{av}}), \quad (26)$$

to control the number of particles N ; the parameter N_{av} controls the mean value of N ; and ν_N governs the rate at which the SGLE equilibrates. We solve the SGLE by using a pseudospectral method, similar to the one described above for the 2D, GP equation, with periodic boundary conditions in space, an implicit-Euler scheme, with time step Δt , for time marching and the method of reference [63] (see page 25 of this reference).

§ Recall that the SGLE can be thought of as an imaginary-time GP equation with external, additive noise (see, *e.g.* reference [38])

	N_c	$k_0(\times\Delta k)$	$\sigma(\times\Delta k)$	g	N_0^i	$\sqrt{D}(\times 10^{-3})$	k_c^{in}	E
A1	1024	5	2	1000	—	—	—	2.120
A2	1024	5	2	2000	—	—	—	3.045
A3	1024	5	2	5000	—	—	—	5.82
A4	1024	35	5	1000	—	—	—	49.69
A5	512	5	2	1000	—	—	—	2.15
A6	256	5	2	1000	—	—	—	2.07
A7	128	5	2	1000	—	—	—	2.1
A8	64	5	2	1000	—	—	—	2.2
A9	256	5	2	2000	—	—	—	2.94
A10	256	5	2	5000	—	—	—	5.57
A11	256	15	2	1000	—	—	—	9.86
A12	256	15	2	2000	—	—	—	10.82
A13	256	15	2	5000	—	—	—	13.68
B1	128	5	1	10000	0.95	—	—	5.44
B2	128	5	1	1000	0.95	—	—	0.59
C1	256	—	—	5000	—	8	6	2.536
C2	256	—	—	1000	—	8	6	0.583
C3	256	—	—	1000	—	10	6	0.637
C4	256	—	—	1000	—	8	9	0.7
C5	256	—	—	1000	—	8	15	1.085
C6	256	—	—	1000	—	8	20	1.557

Table 1. Parameters for our DNS runs A1-A13, B1-B2, and C1-C6: N_c^2 is the number of collocation points, k_0 is the energy-injection scale, σ is the Fourier-space width of $\widehat{\psi}$ at $t = 0$; g is the effective interaction strength; N_0^i is the initial condensate population; D and k_c^{in} are respectively, the variance of the white-noise and the initial value of the truncation wave number, which we use in the initial conditions of type IC3; E is the total energy; we use a square simulation domain of area $\mathcal{A} = L^2$; we choose $L = 32$.

3. Results

We first present the time evolution of the different energies, the probability distribution functions (PDFs) of the velocity components, and the population N_0 in the zero-wave-number mode. We then give a detailed statistical characterization of the temporal evolution of the Fourier-truncated, 2D, GP equation in the four regimes mentioned in the Introduction (section 1).

3.1. Evolution of energies, velocity PDFs, and the zero-wave-number population

We show the early stages of the time evolution of the energies E_{kin}^i , E_{kin}^c , E_{int} , and E_q , from our DNS runs A1-A4, B1, and C6 in figure 1. The runs A1-A4 use initial conditions of type IC1, in which E_{kin}^i is a significant fraction of the total initial energy; the runs B1 and C6 start with initial configurations of type IC2 and IC3, respectively, in which E_{kin}^i is negligibly small at $t = 0$. The transient nature of the early stages of the dynamical

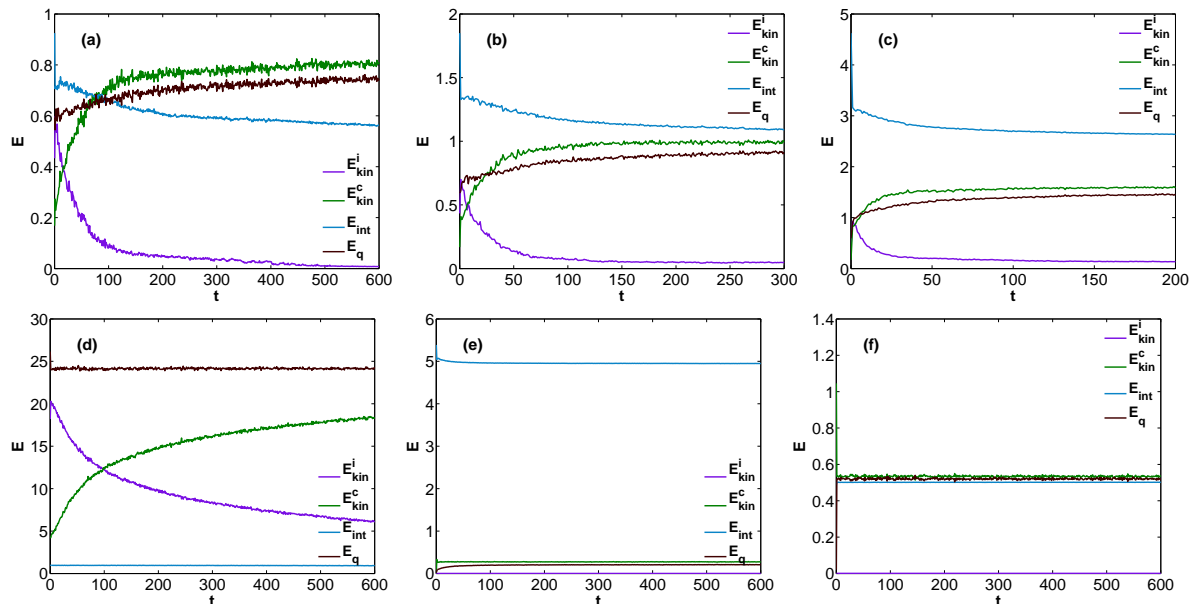


Figure 1. Plots versus time t of the four components of the total energy E_{kin}^i , E_{kin}^c , E_{int} , and E_q , during the initial stages of evolution, from our DNS runs (a) A1, (b) A2 (c) A3, (d) A4, (e) B1, and (f) C6 (see table 1).

evolution of the dissipationless, unforced, 2D, GP equation is evident from figure 1, in which we observe a rapid conversion of E_{kin}^i into the other three components, with a significant fraction being transferred to E_{kin}^c ; moreover, the transient stage depends on the initial conditions, as we describe below. Figures 1 (a)-(c), show comparisons of the temporal evolution of the energies, from the runs A1-A3; we observe, in particular, that the conversion of E_{kin}^i into the other energy components is accelerated as g increases from 1000 to 5000 (cf. [42]); and there is a corresponding acceleration in the approach to thermalization. Moreover, the larger the value of E_{kin}^i the larger is the time required for thermalization, as we can see by comparing figures 1 (a) and (d), for the runs A1 and A4, respectively; the run A4 starts with a high value of $E_{kin}^i(t=0)$ because of a large number of vortices and anti-vortices, so it takes a long time to thermalize; indeed, if the spatial resolution of our DNS is very high, the computational cost of achieving a statistically steady state is prohibitively high for initial conditions A1-A4. In contrast, the runs B1 and C6 have negligibly small values of $E_{kin}^i(t=0)$ to begin with (figures 1 (e) and (f), respectively); and $E_{kin}^i(t)$ remains close to zero throughout the dynamical evolution here. For run B1, both E_{kin}^c and E_q start from values close to zero, grow at the cost of E_{int} , and finally saturate to small, statistically steady values. For run C6, there are hardly any vortices in the initial configuration, so the energies start fluctuating about their statistically steady values very rapidly.

In figure 2 we plot, at three instants of time, the PDFs of v_x and v_y , the Cartesian components of the velocity, for our DNS runs A1, B1, and C6, which correspond, respectively, to initial conditions of types IC1, IC2, and IC3. For the run A1, these PDFs, in figures 2 (a)-(c), show a crossover from a distribution with power-law tails

to one that is Gaussian; the right and left tails of the PDFs in figure 2 (a) can be fit to the form $\sim v_i^{-\gamma}$, with $\gamma \simeq 3.2$, and $i = x$ or y (we show fits only for $i = x$). Such power-law tails in velocity-component PDFs have been seen in experiments [64] and some numerical studies [39, 45, 65, 66]. However, it has not been noted hitherto that, for turbulence in the Fourier-truncated, 2D, GP equation with low-energy initial conditions, such PDFs evolve, as t increases, from PDFs with power-law tails (figure 2 (a) for run A1), to ones with a Gaussian form near the mean, followed by broad tails (figure 2 (b) for run A1), and then to more-or-less Gaussian PDFs (figure 2 (c) for run A1), but with tails that can be fit to an exponential form. This evolution towards Gaussian PDFs is associated with the annihilation of vortices and anti-vortices. The Video S1 in the Supplementary Material shows the temporal evolution of this PDF in the left panel and the spatiotemporal evolution of the pseudocolor plot of the vorticity in the right panel. The analogues of figures 2(a)-(c) for runs B1 and C1, both of which have a negligibly small value of E_{kin}^i at $t = 0$, are given, respectively, in figures 2(d)-(f) and figures 2(g)-(i).

We turn now to the time evolution of the population $N_0(t)$, in the $k = 0$ mode [36, 40, 67], and its dependence on the initial conditions. In figure 3 (a) we plot N_0 versus t for the runs A1-A4 (red, blue, green, and brown curves, respectively), which use initial configurations of type IC1; these figures show that $N_0(t)$ increases with t , on average, and depends on E , g , k_0 , and σ . For the runs A1 and A2 (red and blue curves in figure 3 (a)), $N_0(t)$ approaches a saturation value for the time scales probed by our simulations; figure 3 (a) also shows that, as we increase g (red, blue, and green lines in figure 3 (a)), the fluctuations in N_0 are enhanced and its large- t value, which it seems to approach asymptotically, diminishes. By comparing the runs A1 and A4 (red and brown lines in figures 3 (a)), we see that the latter has a higher value of E than the former, because both k_0 and σ are smaller for A1 than for A4; thus, $N_0(t)$ grows more slowly in A4 than in A1; and, after an equal amount of simulation time, its value in A4 is nearly an order of magnitude lower than in A1; the former shows large fluctuations in $N_0(t)$ and no sign of saturation. The run B1 (figure 3 (e)) uses an initial configuration of type IC2, with a large value of $N_0(t = 0) = 0.95$; in this case, after a period of initial transients, $N_0(t) \rightarrow 0.98$ over our simulation time. The run C6 (figure 3 (f)) uses an initial condition of type IC3; here $N_0(t)$ fluctuates slightly but remains close to its initial value (cf. [40, 67]).

To study the dependence of $N_0(t)$ on the number of collocation points N_c^2 , we evolve the initial configuration of A1 for $N_c = 512$ (run A5), $N_c = 256$ (run A6), $N_c = 128$ (run A7), and $N_c = 64$ (run A8). Figure 3 (g) shows plots of $N_0(t)$ versus t for these five runs; clearly, the initial evolution of $N_0(t)$ depends significantly on N_c ; however, the large- t values of $N_0(t)$, on the time scales of our runs, are comparable ($\simeq 0.9$) for the runs with $N_c = 128$ (run A7), $N_c = 256$ (run A6), and $N_c = 1024$ (run A1). In contrast, the saturation value for the run with $N_c = 64$ (run A8) is $\simeq 0.8$. For the run A5 ($N_c = 512$), $N_0(t)$ shows large fluctuations and no sign of saturation over the time scale that we have covered; this suggests that $N_0(t)$ also depends on the realisation of the random phases

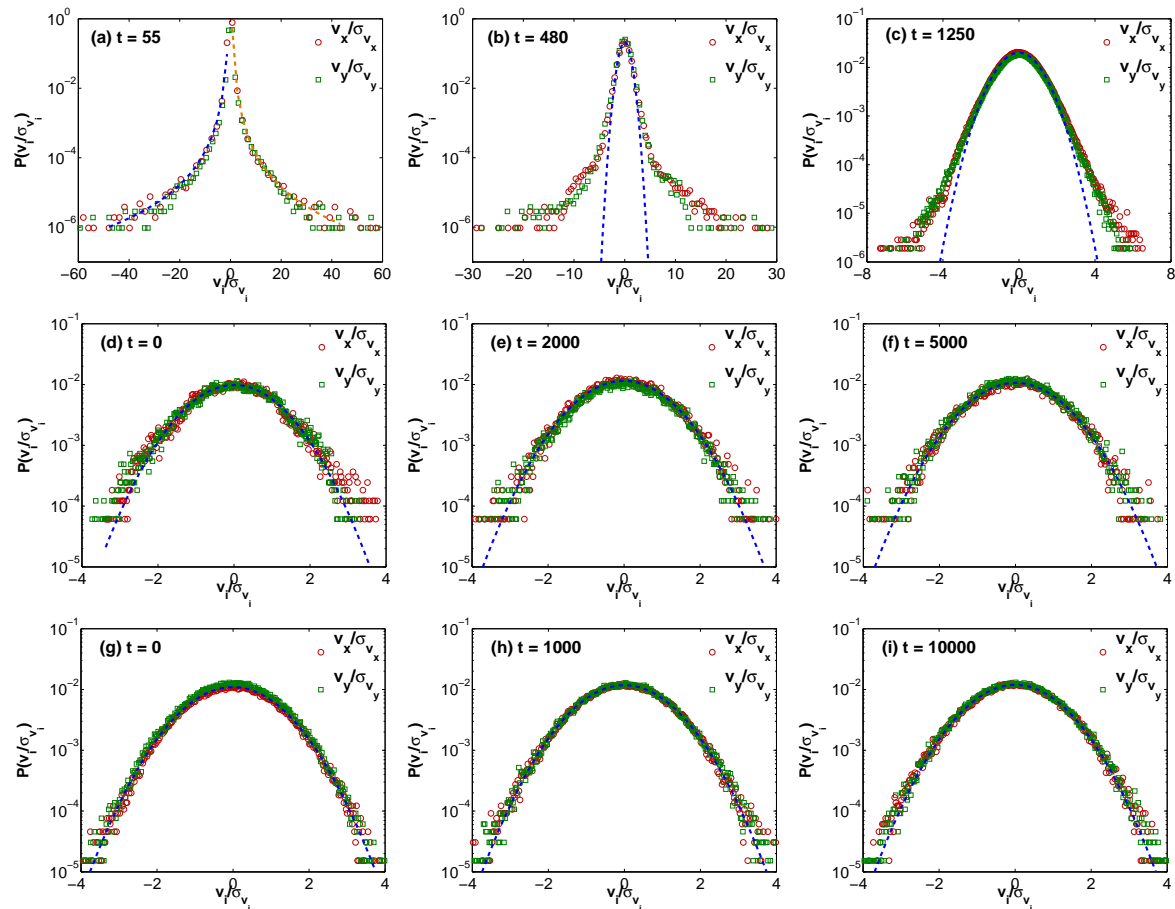


Figure 2. Semilog (base 10) plots of the PDFs of the x (red circles) and y (green squares) components of the velocity from our DNS runs: (a)-(c) A1, (d)-(f) B1, and (g)-(i) C6, corresponding to each of the three types of initial conditions IC1, IC2, and IC3, respectively. The complete time evolution of the PDFs (a)-(c) for the run A1 is illustrated in the top-left panel of the video S1 (supplementary material). The blue-dashed lines in (b)-(i) indicate fits to Gaussian PDFs; the dashed lines in (a) indicate power-law fits to the left (blue-dashed line) and right (orange-dashed line) tails of the PDFs (see text).

$\Theta(k_x, k_y)$ in (21). These plots of $N_0(t)$ illustrate that complete thermalization proceeds very slowly for N_0 ; in the completely thermalized state of the Fourier-truncated, 2D, GP system, N_0 must vanish in the thermodynamic limit by virtue of the Hohenberg-Mermin-Wagner theorem [57, 58]; however, it is not easy to realize this limit in finite-size systems and with the limited run times that are dictated by computational resources. We discuss these issues again in section 3.4 and also refer the reader to [67, 68].

3.2. Initial transients and the onset of thermalization

The initial stages of the evolution of energy spectra for the Fourier-truncated, 2D, GP equations are qualitatively different for initial conditions of types IC1, IC2, and IC3.

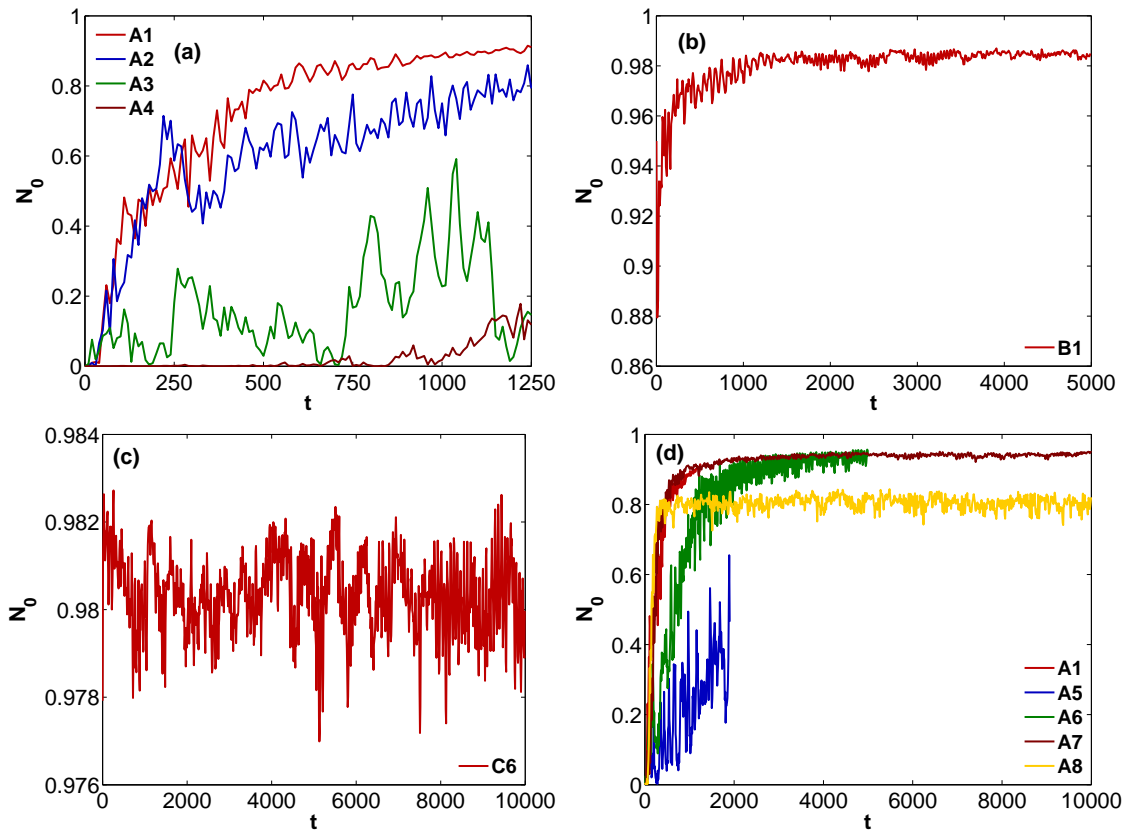


Figure 3. Plots versus time t of the population N_0 , in the zero-wave-number mode, from our DNS runs (a) A1-A4 (initial condition of type IC1), (b) B1 (initial condition of type IC2), (c) C6 (initial condition of type IC3), and (d) A1 and A5-A8, for five values for the number of collocation points N_c^2 , namely, 1024^2 , 512^2 , 256^2 , 128^2 , and 64^2 .

The first type begins with a sizeable incompressible kinetic energy spectrum $E_{kin}^i(k)$; and the initial transients are associated with the annihilation and creation of vortex-antivortex pairs, the associated depletion of $E_{kin}^i(k)$, and the growth of the other energy components [41]. In contrast, runs with initial conditions of types IC2 and IC3 start with a very small incompressible-energy component, therefore, even the early stages of their dynamical evolution are akin to the late stages of the dynamical evolution with initial conditions of type IC1. In figures 4 (a)-(d) we show the time evolution of the spectra $E_{kin}^i(k)$, for the runs A1, A2, A3, and A4, to ascertain the presence of scaling behaviour, if any. We find that, in the low- k region, $E_{kin}^i(k)$ lacks a well-defined scaling region (unlike in [42]); indeed, this region depends on the initial configuration, changes continuously with time, and, in particular, a $k^{-5/3}$ scaling region is tenable (a) over a range of wave numbers that is very tiny and (b) over a fleetingly short interval of time (around $t = 50$ for the run A1). At large wave numbers, $E_{kin}^i(k) \sim k^{-3}$, during the initial stages of evolution, because of the presence of the vortices [44]; this power-law form holds over the same time scales for which the PDF $P(v_x/\sigma_{v_x}) \sim v_x^{-\gamma}$ (figures 2

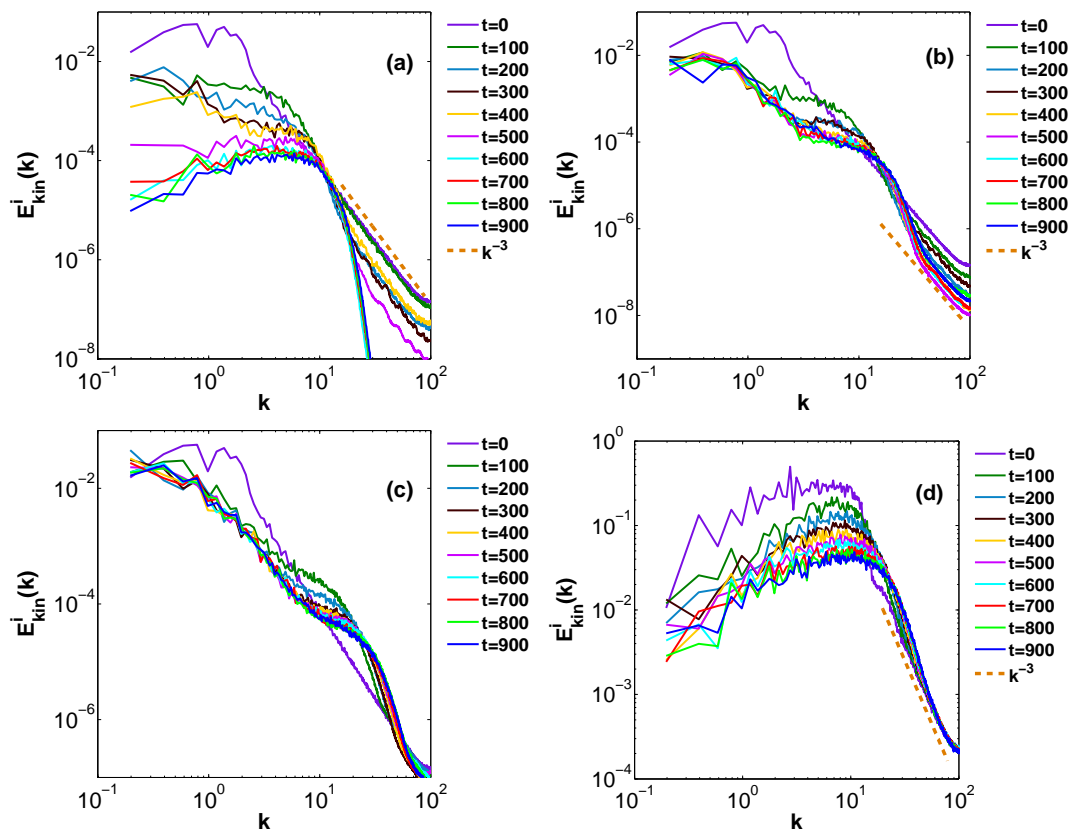


Figure 4. Log-log (base 10) plots of the spectra $E_{kin}^i(k)$ from our DNS runs (a) A1, (b) A2, (c) A3, and (d) A4 at different times t (indicated by curves of different colours); a k^{-3} power law is shown by orange-dashed lines. The complete time evolution of the spectra in (a), (b), (c), and (d) is illustrated in the video S2 (supplementary material).

(a)-(b)).

The initial transients described above are followed by a regime in which the energy and occupation-number spectra begin to show power-law-scaling behaviours, but the power-law exponent and the extent of the scaling region change with time and depend on the initial conditions; we regard this as the onset of thermalization, which is shown in figures 5 and 6, where we illustrate the time evolution of E_{kin}^c . Figure 5 (a) shows $E_{kin}^c(k)$ for the run A1; we begin to see a power-law region here with $E_{kin}^c(k) \sim k$, on the low- k side of the peak after which the spectrum falls steeply. A similar $E_{kin}^c(k) \sim k$ behaviour starts to emerge in the region $k \lesssim k_{max}$ for the run B1 (figure 5 (g)). In this onset-of-thermalization regime, we also see the development of the following power laws: $E_{int}(k) + E_q(k) \sim k$ (figure 7) and $n(k) \sim 1/k$ (figure 8).

3.3. Partial thermalization and self-truncation

3.3.1. Partial thermalization In the third stage of the dynamical evolution of the 2D, Fourier-truncated, GP equation, which we refer to as the partial-thermalization stage,

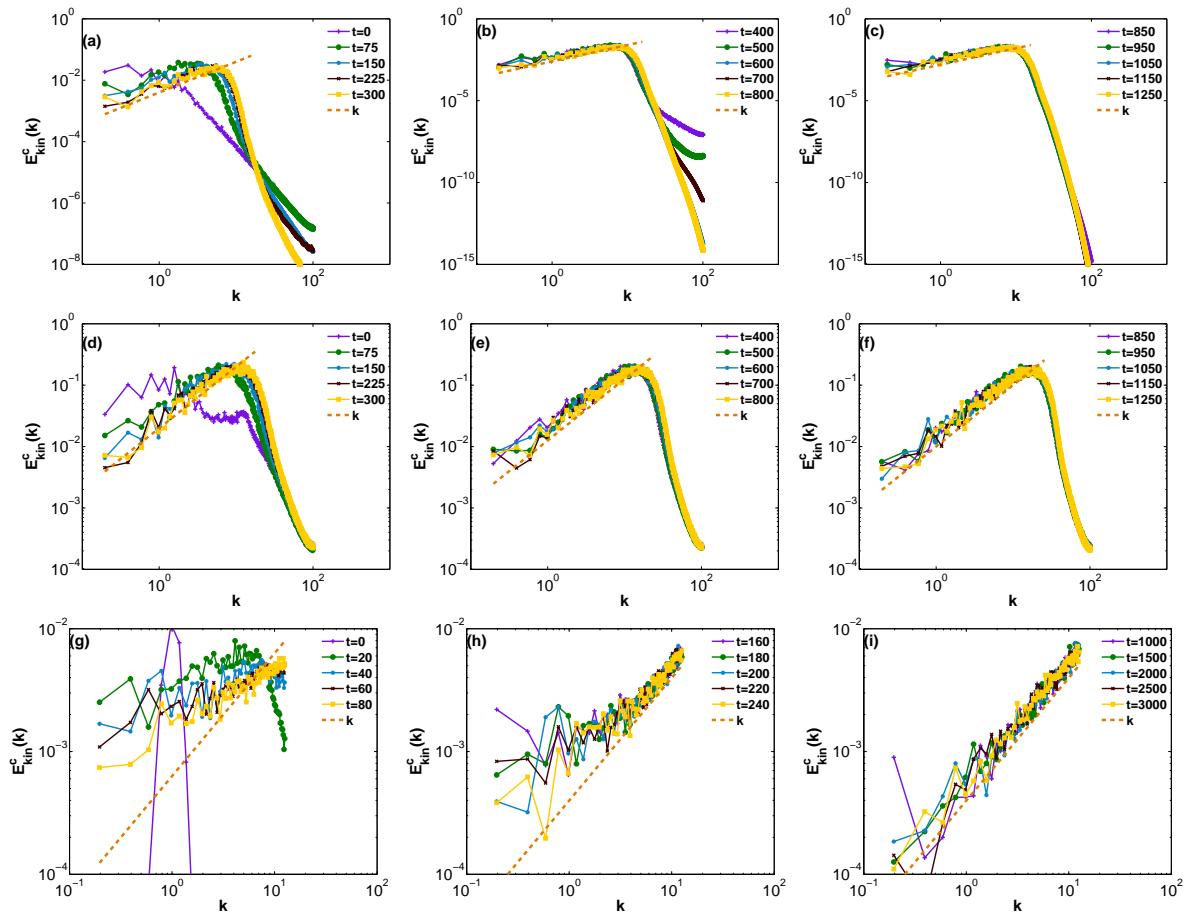


Figure 5. Log-log (base 10) plots of the spectra $E_{kin}^c(k)$ from our DNS runs (a)-(c) A1, (d)-(f) A4, and (g)-(i) B1 at different times t (indicated by curves of different colours); a k power law is shown by orange-dashed lines.

well-defined, power-law-scaling behaviours appear in energy and occupation-number spectra, with exponents that are independent of the initial conditions as illustrated by the compressible-kinetic-energy spectra in figures 5 (b), (c) (e), (f), and 6 (b) for initial conditions of type IC1, and figures 5 (h) and 6 (e), and (f), for initial conditions of type IC2. It is important to distinguish between (I) spectra that fall steeply at large values of k , e.g., the spectra in figures 5 (b), (c) (e), (f), and 6 (e) and (f), and (II) spectra that increase all the way to k_{max} , e.g., the spectra in figures 5 (h) and 6 (b) and (c). In case (I), we have spectral convergence to the 2D GP partial differential equation (PDE); in case (II), the effects of Fourier truncation are so pronounced that our truncated 2D, GP system does not provide a good representation of the 2D, GP PDE. As we show below, case (I) can be further subdivided into (A) a subclass in which the maximum, at $k = k_c$ in $E_{kin}(k) = (E_{kin}^c(k) + E_{kin}^i(k))$, referred to as the self-truncation wave number [51], moves out to k_{max} as a power of t and (B) a subclass in which k_c moves out to k_{max} at a rate that is slower than a power of t .

Figures 5 (g)-(i), from the run B1, show how $E_{kin}^c(k)$ evolves as the spectral

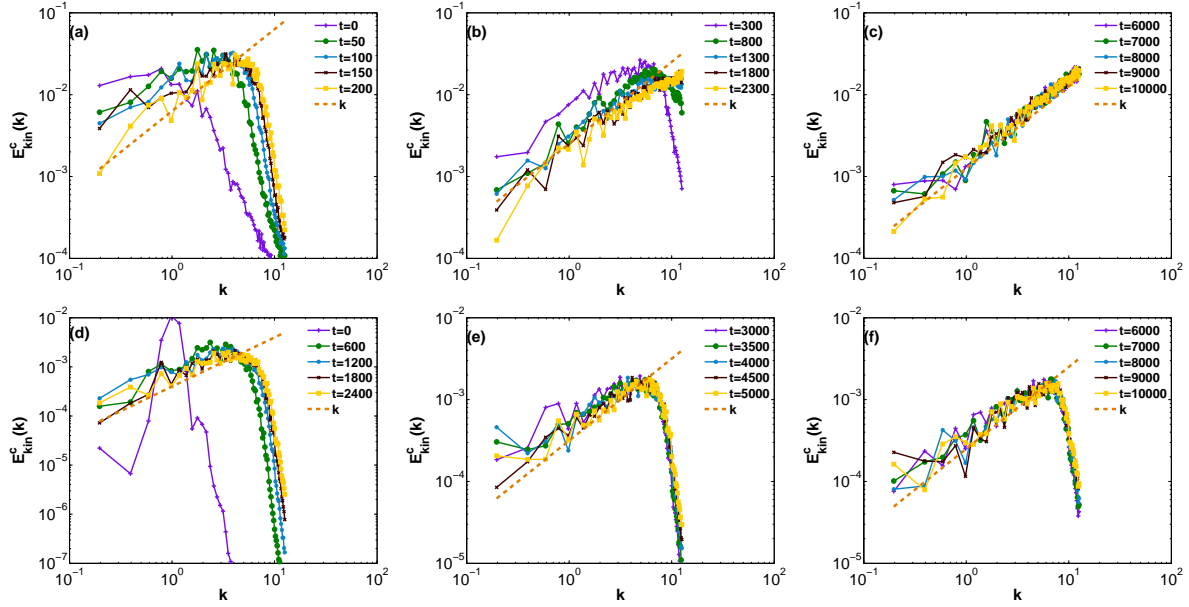


Figure 6. Log-log (base 10) plots of the spectra $E_{kin}^c(k)$ from our DNS runs (a)-(c) A7 and (d)-(f) B2 at different times t (indicated by curves of different colours); a k power law is shown by orange-dashed lines.

convergence to the GP PDE is lost in case (II); note that the scaling region with $E_{kin}^c \sim k$ sets in at high wave numbers close to k_{max} and then extends to the low-wave-number regime. For case (IA) analogous plots of $E_{kin}^c(k)$ are given in, e.g., figures 6 (a)-(c). We give plots for case (IB) in the next subsection, where we study in detail the time dependence of k_c . Illustrative plots of the spectra $(E_i(k) + E_q(k))$ and $n(k)$ in this regime of partial thermalization are given in figures 7 and 8, respectively.

3.3.2. Self-truncation We now present a detailed characterization of the partial-thermalization regime, when energy spectra display self-truncation at wave-numbers beyond $k_c(t)$, which can be defined as follows:

$$k_c = \sqrt{\frac{2 \int_0^{k_{max}} k^2 E_{kin}(k) dk}{\int_0^{k_{max}} E_{kin}(k) dk}}; \quad (27)$$

as the system approaches complete thermalization, $k_c(t) \rightarrow k_{max}$. In particular, we explore how the scaling ranges in energy spectra grow with t for different values of g , with the initial configuration and number of collocation points N_c held fixed. For an initial condition of type IC1, with $k_0 = 5\Delta k$, $\sigma = 2\Delta k$, and $N_c = 256$, we obtain the time evolution of energy spectra for $g = 1000$ (run A6), $g = 2000$ (run A9), and $g = 5000$ (run A10) in figures 9 (a), (b), and (c), respectively, and their video analogues (Videos S3 (panel V2) in the Supplementary Material). The larger the value of g , the more rapid is the thermalization, and the consequent loss of spectral convergence, as we can

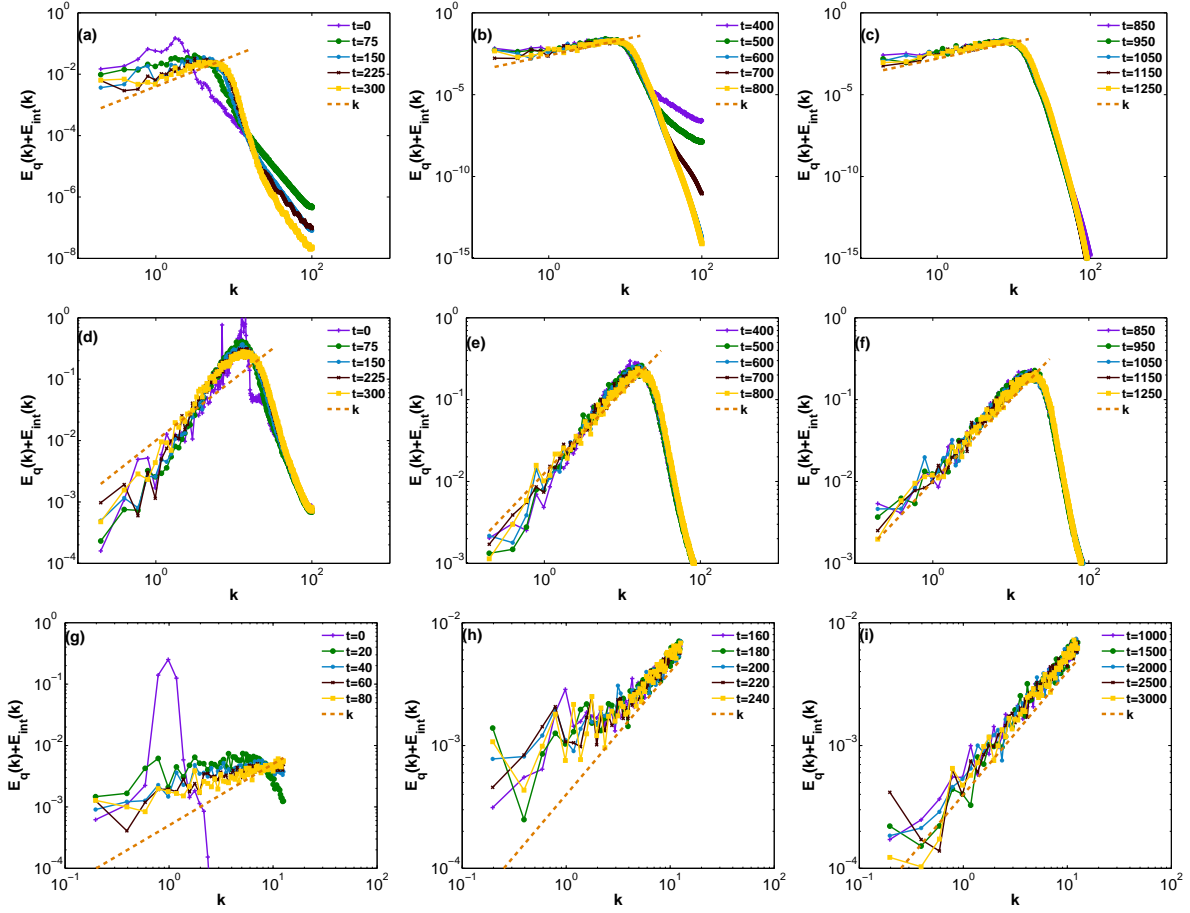


Figure 7. Log-log (base 10) plots of the spectra $E_{int}(k) + E_q(k)$ from our DNS runs (a)-(c) A1, (d)-(f) A4, and (g)-(i) B1 at different times t (indicated by curves of different colours); a k power law is shown by orange-dashed lines.

see by comparing the sky-blue (run A10), green (run A9), and purple (run A6) spectra in figures 9 (a)-(c); run A6 loses spectral convergence around $t = 2500$. We obtain the same qualitative g dependence, with $k_0 = 15\Delta k$, $\sigma = 2\Delta k$, and $N_c = 256$, for $g = 1000$, 2000, and 5000, i.e., runs A11, A12, and A13, respectively, for which energy spectra are portrayed in figures 9 (d)-(f) and Video S3 (panel V3) in the Supplementary Material.

In figures 9 (g)-(i) we explore the N_c dependence of the self-truncation of energy spectra, for initial conditions, with $k_0 = 5\Delta k$, $\sigma = 2\Delta k$, and $g = 1000$, and five different values of N_c , namely, $N_c = 1024$ (run A1), 512 (run A5), 256 (run A6), 128 (run A7), and 64 (run A8). We find, not surprisingly, that the lower the value of N_c the more rapidly does the system lose spectral convergence.

Initial conditions of type IC2 lead to energy spectra whose time evolution, and their dependence on g and N_c , is similar to those that are obtained from initial conditions of type IC1.

With initial conditions of types IC1 and IC2, we cannot control the initial value $k_c(t = 0) \equiv k_c^{in}$ easily. However, initial conditions of type IC3, which we obtain from

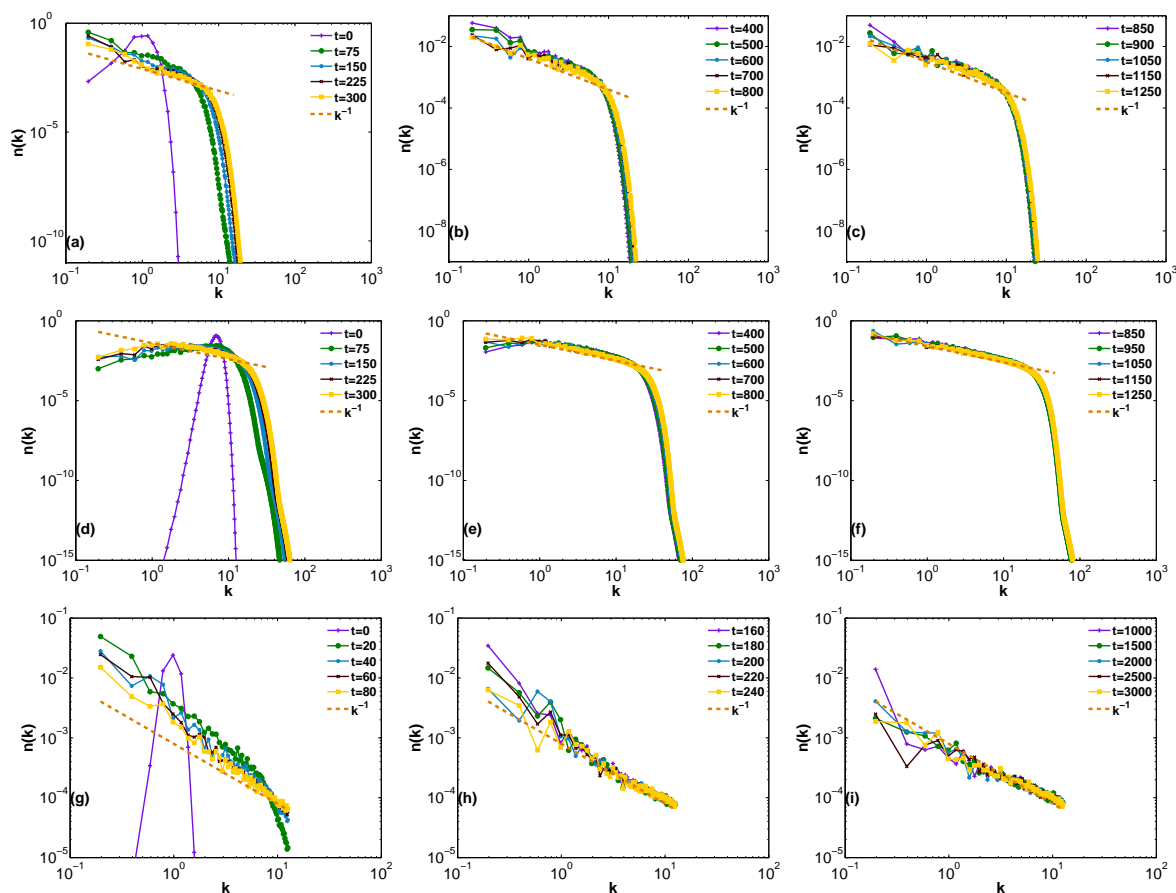


Figure 8. Log-log (base 10) plots of the spectra $n(k)$ from our DNS runs (a)-(c) A1, (d)-(f) A4, and (g)-(i) B1 at different times t (indicated by curves of different colours); a k^{-1} power law is shown by orange-dashed lines.

the SGLE, allow us to control k_c^{in} and start, therefore, with initial spectra that display partial thermalization for $k < k_c^{in}$ [51] and a sharp fall thereafter. In figure 10 we show the time evolution of $E_{kin}^c(k)$ for such initial conditions from runs C1-C6. For different representative values of k_c^{in} , g , and D , we now study the time evolution of $k_c(t)$, which characterizes the growth of the partially thermalized scaling region. Here too, as with initial conditions of types IC1 and IC2, if all other parameters like $k_c^{in} = 6.0$ and D are held fixed, the speed of thermalization increases with g (cf. figure 10 (a) for the run C1, with $g = 5000$, and figure 10 (b) for the run C2, with $g = 1000$). For these runs C1-C6, the growth of the energy spectra, in the region $k > k_c^{in}$, starts with the smoothing of the sharp cut-off at k_c^{in} ; the higher the value of k_c^{in} , the slower is this growth (cf. figures 10 (b), (d), (e), and (f) for runs C2, C4, C5, and C6, respectively). By contrast, an increase in D (or T) in the SGLE, accelerates this growth (cf. figures 10 (b) and (c) for runs C2 and C3, respectively).

The growth of $k_c(t)$ with t , illustrated in figure 11 (a), can be fit to the form $k_c(t) \sim t^\alpha$; however, as we show below, α depends on the initial condition. We obtain

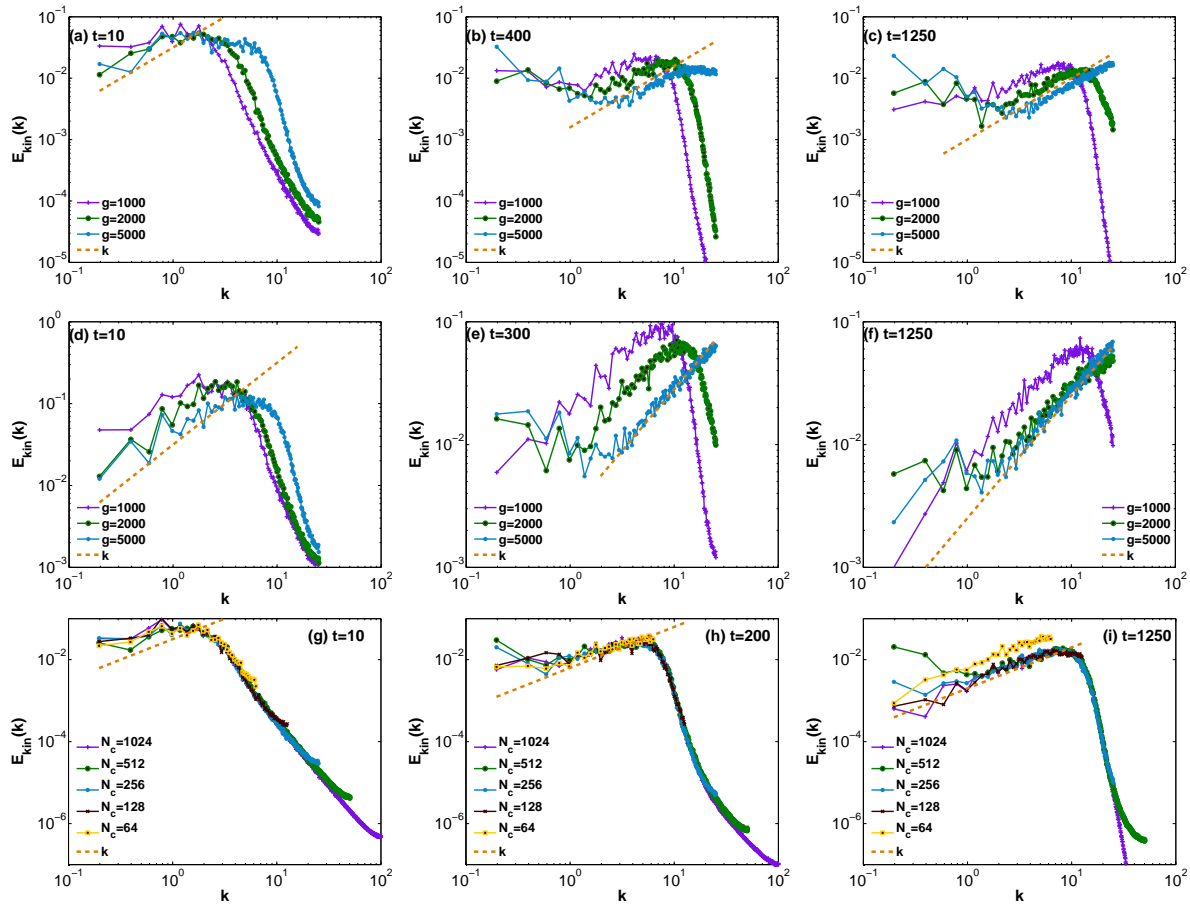


Figure 9. Log-log (base 10) plots of the spectra $E_{kin}(k)$ from our DNS runs (a)-(c) A6, A9, and A10 ($k_0 = 5\Delta k$ and $\sigma = 2\Delta k$), (d)-(f) A11, A12 and A13 ($k_0 = 15\Delta k$ and $\sigma = 2\Delta$), and (g)-(i) A1, A5-A8 ($N_c^2 = 1024^2, 512^2, 256^2, 128^2$, and 64^2). The complete time evolutions of the spectra in (a)-(c), (d)-(f), and (g)-(i) are illustrated in the panels V2, V3, and V4 of video S3.

the exponent α either from slopes of log-log plots of (i) $k_c(t)$ versus t or (ii) dk_c/dt versus k_c/k_{max} ; we denote the values from procedures (i) and (ii) as α_1 and α_2 , respectively. Note that in (ii) we have a parametric plot [38, 51], shown in figure 11 (b); this yields a straight-line scaling regime with slope χ and $\alpha_2 = 1/(1 - \chi)$. The values of α_1 and α_2 , listed in table 2, show that $\alpha_1 \simeq \alpha_2$; the discrepancy between these two values for α is a convenient measure of the errors of our estimates. For runs C4, C5, and C6, we cannot obtain α_2 reliably; the small values of α_1 for these runs indicate very slow growth of $k_c(t)$; indeed, in runs C5 and C6, a case can be made for a logarithmic growth of $k_c(t)$ with t .

3.4. Complete thermalization

The partially thermalized stage of the dynamical evolution of the 2D, Fourier-truncated, GP equation may either gradually become completely thermalized, in which state a

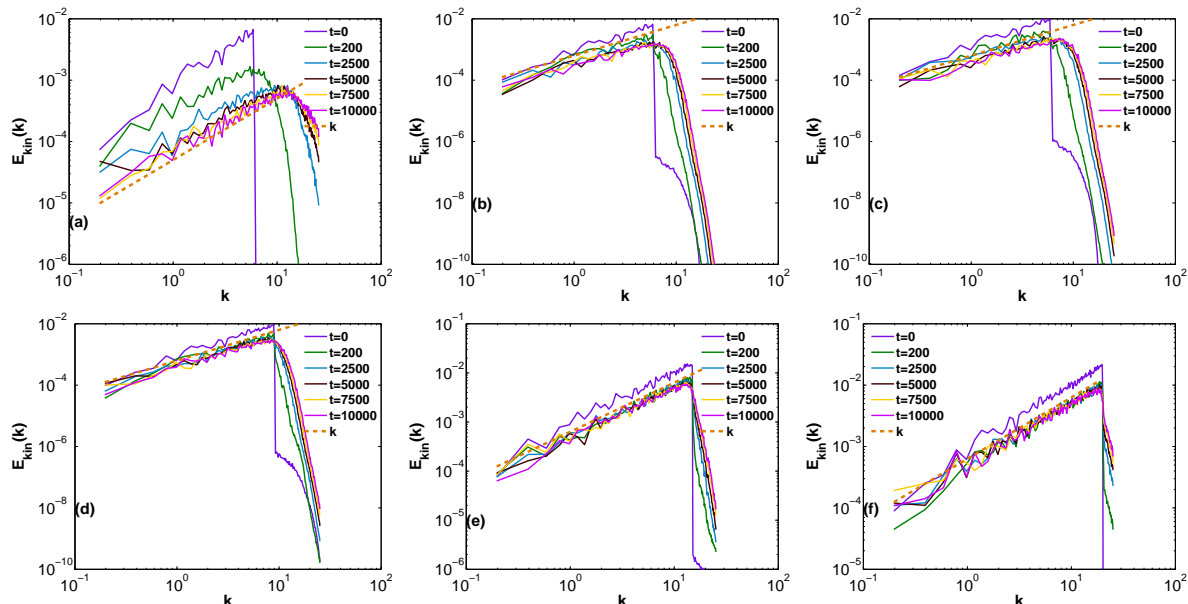


Figure 10. Log-log (base 10) plots of the spectra $E_{kin}(k)$ from our DNS runs (initial conditions of type IC3 (a) C1, (b) C2, (c) C3, (d) C4, (e) C5, and (f) C6).

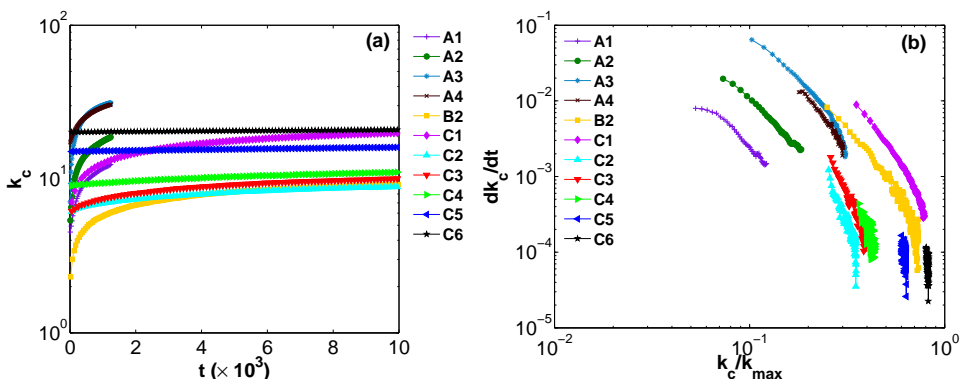


Figure 11. Plots of (a) the self-truncation wave-number $k_c(t)$ versus time t and (b) dk_c/dt versus k_c/k_{max} from our DNS runs A1-A4, B2, and C1-C6.

power-law scaling region is present in the entire energy and the occupation number spectra, or remain self-truncated with logarithmic growth. In figures 5 (g)-(i) and 6 (a)-(c), we show the compressible kinetic energy spectra E_{kin}^c for the runs B1 and A7, where E_{kin}^c shows power-law scaling over the entire wave number range, from $k = 2\pi/L$ up to k_{max} , towards the end of the respective simulations; a naïve fit is consistent with $E_{kin}^c(k) \sim k$ (but see below).

3.4.1. Correlation functions and the BKT transition A uniform, 2D, interacting Bose gas exhibits a BKT phase at low energies (temperatures in the canonical ensemble). Thus, the completely thermalized state of the 2D, Fourier-truncated, GP equation

	E	k_{max}	ξ	ξk_{max}	k_c^i	k_c^f	α_1	α_2
A1	2.120	100.53	1.01	101.73	4.52	12.42	0.28	0.26
A2	3.045	100.53	0.72	71.9	5.39	18.72	0.28	0.28
A3	5.82	100.53	0.45	45.49	7.11	31.3	0.29	0.27
A4	49.69	100.53	1.01	101.73	17.31	30.53	0.2	0.21
B2	0.589	12.57	1.01	12.72	2.23	9.23	0.24	0.25
C1	2.536	25.13	0.45	11.37	7.08	19.91	0.22	0.22
C2	0.583	25.13	1.01	25.43	6.15	8.90	0.12	0.14
C3	0.637	25.13	1.01	25.43	6.18	10.05	0.14	0.15
C4	0.6999	25.13	1.01	25.43	9.05	11.07	0.09	–
C5	1.085	25.13	1.01	25.43	15.09	16.08	0.04	–
C6	1.557	25.13	1.01	25.43	20.17	20.87	0.02	–

Table 2. Summary of the self-truncation results from our DNS runs A1-A4, B2, and C1-C6: E is the total energy; $k_{max} = 2\pi N_c/2L$; $\xi = L/\sqrt{g}$ is the healing length; k_c^i and k_c^f are the initial and final values of k_c (averaged over a few time steps); α_1 is the slope obtained from the log-log (base 10) plot of k_c versus t and $\alpha_2 = 1/(1 - \chi)$, where χ is the slope obtained from the log-log (base 10) plot of dk_c/dt versus k_c/k_{max} .

should yield a BKT phase [52,54], with the correlation function $c(r) \sim r^{-\eta}$, at energies $E < E_{BKT}$; and $c(r)$ should decay exponentially with r if $E > E_{BKT}$. We show this explicitly now by using initial conditions of type IC1 with $N_c = 64$ and $N_c = 128$ and $g = 1000$; we obtain different energies by changing k_0 and σ (runs D1-D13 and E1-E12 in table 3).

In figure 12, we present plots of the correlation functions $c(r)$. To illustrate the BKT transition clearly, we present log-log plots of $c(r)$ versus r , for $E < E_{BKT}$, in figures 12 (a) and (d), where the straight lines indicate power-law regimes; and, for $E > E_{BKT}$, we use semi-log plots, as in figures 12 (b) and (e), where the straight lines signify an exponential decay of $c(r)$ with r . Given the resolution of our DNS runs, we find that, in a small energy range in the vicinity of E_{BKT} , we cannot fit power-law or exponential forms satisfactorily; this leads to an uncertainty in our estimate for E_{BKT} . Aside from this uncertainty, the behavior of $c(r)$, in the regime of complete thermalization, is in accord with our expectations for the BKT phase; in particular, the exponent η (see equation (18)) depends on E for $E < E_{BKT}$ as shown in figures 12 (c) and (f). Our values for η , for the runs with $E < E_{BKT}$ and with $N_c = 64$ and $N_c = 128$, are listed in table 3. Note that $E_{BKT} \simeq 6(N_c = 64)$ and $E_{BKT} \simeq 19(N_c = 128)$, i.e., E_{BKT} depends on N_c , the number of collocation points; we show analytically below how a low-temperature analysis can be used to understand this dependence of E_{BKT} on N_c . In the completely thermalized state of the Fourier-truncated, 2D, GP system, N_0 must vanish in the thermodynamic limit by virtue of the Hohenberg-Mermin-Wagner theorem [57,58] and $n(k) \sim k^{-1+\eta}$; it is not easy to realize this limit in finite-size systems and with the limited run times that are dictated by computational resources (see the plots of N_0 in figure 3); however, finite-size scaling can be used to extract the exponent η from the

$N_c = 128$	k_0 ($\times \Delta k$)	σ ($\times \Delta k$)	E	η	$N_c = 64$	k_0 ($\times \Delta k$)	σ ($\times \Delta k$)	E	η
D1	5	2	2.1	0.008	E1	0	2	1.12	0.012
D2	10	2	5.05	0.024	E2	3	2	1.64	0.025
D3	12	2	6.74	0.034	E3	5	2	2.2	0.040
D4	14	2	8.74	0.047	E4	8	2	3.68	0.083
D5	16	2	11.05	0.080	E5	10	2	5.04	0.164
D6	18	2	13.68	0.111	E6	11	2	5.84	0.255
D7	20	2	16.62	0.181	E7	12	2	6.75	
D8	21	2.5	18.34	0.239	E8	13	2	7.74	
D9	24	3	23.75		E9	14	2	8.78	
D10	25	2	25.3		E10	15	2	9.88	
D11	26	2	27.27		E11	16	2	11.05	
D12	28	2	31.44		E12	17	2	12.32	
D13	30	2	35.9						

Table 3. List of parameters for our complete-thermalization DNS runs D1-D13 ($N_c^2 = 128^2$) and E1-E12 ($N_c^2 = 64^2$): N_c^2 is the number of collocation points; k_0 is the energy-injection scale; σ is Fourier-space width of ψ at $t = 0$; E is the total energy; and η is the exponent of the correlation function $c(r) \sim r^{-\eta}$ for $E < E_{BKT}$. $g = 1000$ for all the DNS runs and they have been performed on a square simulation domain of area $\mathcal{A} = L^2$, with $L = 32$.

$k = 0$ part of $n(k)$ as shown in reference [68]; similarly, $E_{kin}^c(k)$ should also show a power-law form with an exponent that depends on η , but this is difficult to realize in numerical calculations with limited spatial resolutions and run lengths.

3.4.2. Analytical estimation of the energy of the BKT transition The energy of a pure condensate of a uniform, weakly interacting, 2D Bose gas, which is described by the GP equation (1), is $E_0 = g/(2\mathcal{A})$. We define the energy of our system to be $E = E_0(1 + \delta\mathcal{E})$; this energy E is fixed by the initial condition; and $\delta\mathcal{E}$ measures the relative amount by which E exceeds E_0 . As we show in the Appendix B, the N_c dependence of the energy E_{BKT} , at which the BKT transition occurs, can be obtained approximately as follows. We begin with

$$\delta\mathcal{E}_{BKT} = \delta\tilde{\mathcal{E}}_{BKT} \frac{8}{\log(\pi^2 N_c^2 \left(1 + \frac{\pi^2 N_c^2}{2g}\right))}, \quad (28)$$

where $\delta\tilde{\mathcal{E}}_{BKT}$, the estimate for the BKT transition energy that follows from an energy-entropy argument (see (20) in the Appendix and [52]), is

$$\delta\tilde{\mathcal{E}}_{BKT} = \frac{\pi^2 N_c^2}{2g} = \frac{\xi^2 k_{\max}^2}{2}, \quad (29)$$

whence we obtain

$$\delta\mathcal{E}_{BKT} = \frac{4 k_{\max}^2 \xi^2}{\log(k_{\max}^2 \mathcal{A} \left(1 + \frac{k_{\max}^2 \xi^2}{2}\right))}. \quad (30)$$

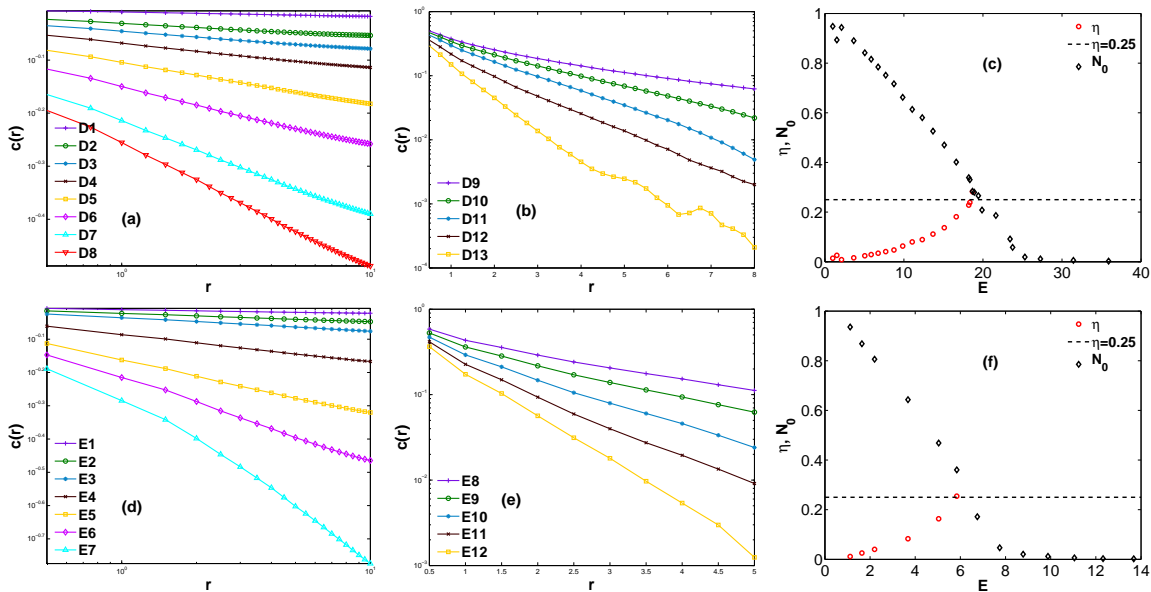


Figure 12. Plots of $c(r)$ versus r for different energies in the complete-thermalization regime, for $N_c^2 = 128^2$ ((a) and (b)) and $N_c^2 = 64^2$ ((d) and (e)). (a) and (d) Log-log (base 10) plots of $c(r)$ versus r for different energies $E < E_{KT}$; the slopes of the linear parts of these plots yield the exponent η (table 3); (b) and (e) semilog (base(10) plots of $c(r)$ versus r for different energies $E > E_{KT}$; (c) ($N_c^2 = 128^2$) and (f) ($N_c^2 = 64^2$) show plots of η and N_0 versus E (on the time scales of our runs N_0 is nonzero; see the text for a detailed discussion).

N_c	E_0	$\delta\tilde{\mathcal{E}}_{\text{BKT}}$	$\delta\mathcal{E}_{\text{BKT}}$	$E_{\text{BKT}}^{\text{A}}$	$E_{\text{BKT}}^{\text{DNS}}$
64	0.488	20.21	11.84	6.27	5.84
128	0.488	80.85	39.44	19.75	18.34

Table 4. The values of E_0 , $\delta\tilde{\mathcal{E}}_{\text{BKT}}$ (see (29)), $\delta\mathcal{E}$ (see (30)), $E_{\text{BKT}}^{\text{A}}$ (see (31)), and $E_{\text{BKT}}^{\text{DNS}}$ from our DNS runs D1-D13 ($N_c = 64$) and E1-E12 ($N_c = 64$). E_0 is the ground state energy of a pure condensate of a uniform, interacting, 2D Bose gas and $E_{\text{BKT}}^{\text{DNS}}$ is BKT-transition energy determined using our DNS runs.

We can now write

$$E_{\text{BKT}} = E_0 \left(1 + \frac{4\pi^2 N_c^2}{g \log(\pi^2 N_c^2 (1 + \frac{\pi^2 N_c^2}{2g}))} \right); \quad (31)$$

by using this expression we can determine the ratio $E_{\text{BKT}}(N_c^a)/E_{\text{BKT}}(N_c^b)$ for runs with two different values, N_c^a and N_c^b , for the number of collocation points; we can also obtain this ratio from our DNS, by determining the value of E at which the exponent η becomes $1/4$. In Table 4 we compare $E_{\text{BKT}}(N_c)$ for $N_c = 64$ and $N_c = 128$; our analytical approximation (31) yields $E_{\text{BKT}}^{128}/E_{\text{BKT}}^{64} \simeq 3.15$; this is in excellent agreement with the value $\simeq 3.14$ that we obtain for this ratio from our DNS results.

4. Conclusions

We have carried out an extensive study of the statistical properties of the dissipationless, unforced, 2D, Fourier-truncated, GP equation. Our study has been designed specifically to study and identify the universal features, if any, of the turbulent evolution of the solutions of this equation, by undertaking a systematic DNS. In our study, we have used statistical measures such as velocity-component PDFs and energy and occupation-number spectra, for a large number of initial conditions. To the best of our knowledge, such a comprehensive study of the Fourier-truncated, 2D, GP equation has not been attempted hitherto.

Our comprehensive study of the Fourier-truncated, 2D, GP equation, which makes use of the three types of initial conditions (section 2.2) and a wide range of parameters (tables 1 and 3), allows us to systematize the dynamical evolution of this system into four different regimes, with qualitatively different statistical properties. This demarkation of the evolution into different regimes has not been systematized in earlier studies, which have concentrated only on one or two of these regimes. For example, the study of reference [39] has investigated states with a significant number of vortex-antivortex pairs and obtained for them PDFs of velocity components that have power-law tails of the type shown in figure 2. References [47, 54, 68] have investigated the BKT nature of the thermalized state. Wave-turbulence studies [32, 41, 69] have focussed on power-law regions in energy and occupation-number spectra of the type we find in our third regime. The DNS studies in [41–45, 70] have considered the time evolution of spectra and PDFs for the Fourier-truncated, 2D, GP equation; in some cases, these studies introduce dissipation or hyperviscosity and forcing; they have also reported different power laws in spectra [42, 43, 45]. Our work suggests that, at least in the dissipationless, unforced, Fourier-truncated, 2D, GP equation, the only robust power laws in spectra are the ones we have reported above; all other apparent power laws occur either (a) for very special initial conditions [44] or (b) last for fleetingly small intervals of time and extend over very small ranges of k .

To recapitulate, we find that, in the first dynamical-evolution regime of the Fourier-truncated, 2D, GP equation, there are initial-condition-dependent transients. In the second regime the energy and the occupation-number spectra start to develop power-law scaling regions, but the power-law exponent and the extent of the scaling region change with time and are influenced by the initial conditions. In the third regime, of partial thermalization, we find $E_{kin}^c(k)$ and $E_{int}(k) + E_q(k) \sim k$, and $n(k) \sim 1/k$, for $k < k_c(t)$ and, for $k > k_c$, we find an initial-condition-dependent self-truncation regime, in which the spectra drop rapidly; the self-truncation wave number $k_c(t)$ grows either as t^α or logarithmically for different initial conditions (table 2). In the fourth, complete-thermalization regime, power-law forms of correlation functions and spectra, for $E < E_{BKT}$, are consistent with their nontrivial BKT forms; however, considerable care must be exercised, as explained in section 3.4.1 and [47, 54, 68], to distinguish these nontrivial power laws from their wave-turbulence analogs [32, 41, 69].

Acknowledgments

We thank CSIR, DST, and UGC(India) for financial support, and SERC (IISc) for computational resources.

Appendix A.

The GP equation, which describes the dynamical evolution of the wave function $\psi(\mathbf{x}, t)$ of a weakly interacting, 2D Bose gas at low temperatures, is

$$i\hbar \frac{\partial \psi(\mathbf{x}, t)}{\partial t} = -\frac{\hbar^2}{2m} \nabla^2 \psi(\mathbf{x}, t) + g_{2D} |\psi|^2 \psi(\mathbf{x}, t), \quad (\text{A.1})$$

where g_{2D} is the effective interaction strength. As we have mentioned earlier (see (2) and (3)), the GP equation conserves the energy, given by the Hamiltonian

$$H = \int_{\mathcal{A}} d^2x \left(\frac{\hbar^2}{2m} |\nabla \psi|^2 + \frac{g_{2D}}{2} |\psi|^4 \right), \quad (\text{A.2})$$

and the total number of particles $n = \int_{\mathcal{A}} |\psi|^2 d^2x$. To obtain (1), we first divide (A.1) by \hbar and define $g = g_{2D}/\hbar$; we then set $\hbar/2m = 1$, with $m = 1$, so that $|\psi|^2$ is the same as ρ ; this is tantamount to using units with $\hbar = 2$.

Appendix B.

The Berezinskii-Kosterlitz-Thouless (BKT) transition is best studied by using the renormalization group [52]; here, we restrict ourselves to the heuristic, energy-entropy argument to obtain a rough estimate of the BKT transition temperature T_{BKT} . In the XY model, this transition is studied by using the Hamiltonian

$$H_{\text{XY}} = -J \sum_{\langle i,j \rangle} \cos(\theta_i - \theta_j), \quad (\text{B.1})$$

where $\langle i, j \rangle$ denotes nearest-neighbour pairs of sites, on a 2D square lattice, J is the nearest-neighbour exchange coupling, and $(\theta_i - \theta_j)$ is the angle between the nearest-neighbour, XY spins on sites i and j . In the continuum limit, the above Hamiltonian becomes, to lowest order in spatial gradients,

$$H_{\text{XY}} = \frac{J}{2} \int d^2x (\nabla \theta(x))^2. \quad (\text{B.2})$$

By comparing (B.2) with the kinetic-energy term in (A.1), we find that

$$J = \frac{|\langle \psi \rangle|^2 \hbar^2}{m} = \frac{\rho \Gamma^2}{(2\pi)^2}, \quad (\text{B.3})$$

where Γ denotes the Onsager-Feynman quantum of velocity circulation $\Gamma = 4\pi\hbar/2m = h/m$. A rough estimate for the BKT transition temperature T_{BKT} is given below:

$$\tilde{T}_{\text{BKT}} = \frac{\pi J}{2k_B} = \frac{\pi |\langle \psi \rangle|^2 \hbar^2}{2mk_B} = \frac{\rho \Gamma^2}{8\pi k_B}, \quad (\text{B.4})$$

here \tilde{T}_{BKT} denotes the estimate for T_{BKT} that follows from an energy-entropy argument [52]. For $T < T_{\text{BKT}}$, the phase correlation function $c(r)$ (see (17)) and the angle-integrated spectrum $\hat{c}(k)$, which follows from a Fourier transform of $c(r)$, scale as

$$c(r) \sim (a/r)^{\frac{T}{4T_{\text{BKT}}}} \quad (\text{B.5})$$

and

$$\hat{c}(k) \sim k^{-1 + \frac{T}{4T_{\text{BKT}}}}, \quad (\text{B.6})$$

respectively. Above T_{BKT} the correlation length

$$\ell = \frac{\int k^{-1} E(k) dk}{\int E(k) dk} \quad (\text{B.7})$$

is finite; and, as $T \rightarrow T_{\text{BKT}}$, it displays the essential singularity

$$\ell \sim \exp(b(T_{\text{BKT}}/(T - T_{\text{BKT}}))^{1/2}). \quad (\text{B.8})$$

Appendix B.1.

We now develop an analytical framework, which is valid at low-temperatures $T \ll T_{\text{BKT}}$, that can be used to test some of the results of our DNS runs in the region of complete thermalization. We first calculate equilibrium thermodynamic functions for a weakly-interacting, 2D Bose gas, in the grand-canonical ensemble; we then obtain their analogues in the microcanonical ensemble. In the grand-canonical ensemble the probability of a given state is

$$\mathbb{P} = \frac{1}{\Xi} e^{-\beta(H - \mu N)}, \quad (\text{B.9})$$

where Ξ is the grand partition function, β the inverse temperature, μ the chemical potential, and N the number of bosons. The grand-canonical potential is

$$\Omega = -\beta^{-1} \log(\Xi); \quad (\text{B.10})$$

and the mean energy E , entropy S , and N are

$$N = -\frac{\partial \Omega}{\partial \mu}, \quad (\text{B.11a})$$

$$S = \beta^2 \partial \Omega / \partial \beta, \quad (\text{B.11b})$$

$$E = \frac{\partial \Omega}{\partial \beta} + \mu N = \frac{S}{\beta} + \mu N. \quad (\text{B.11c})$$

We adapt to 2D the 3D study of Ref. [51], expand ψ in terms of Fourier modes $A_{\mathbf{k}}$, and obtain Ω as the sum of the saddle-point part Ω_{sp} and Ω_Q , the deviations from the saddle point that are quadratic in $A_{\mathbf{k}}$. We write $\Omega = \Omega_{sp} + \Omega_Q$, where $\Omega_{sp} = -\mathcal{A}\mu^2/2g$ and

$$\Omega_Q = - \int_0^{p_{\max}} \frac{\left(p \mathcal{A} \log\left(\frac{2m}{\beta \sqrt{p^4 + 4mp^2\mu}} \right) \right)}{2\pi \beta \hbar^2}. \quad (\text{B.12})$$

We can also calculate the condensate depletion δN , where the particle number $N = N_0 + \delta N$ and N_0 is the number of particles in the $k = 0$ mode, as follows:

$$\delta N = \int_0^{p_{\max}} \frac{mp\mathcal{A} \left(p^{-2} + \frac{1}{p^2 + 4m\mu} \right)}{2\pi\beta\hbar^2}. \quad (\text{B.13})$$

The integrals in the (B.12) and (B.13) can be performed analytically, but, in contrast to the 3D case where the primitives are zero at $p = 0$, the 2D primitive for Ω_{ph} is finite at $p = 0$ and for δN it is infra-red (I.R.) divergent. By subtracting the I.R. finite and divergent terms from Ω_Q and δN , respectively, we get the following expressions, in 2D, in the thermodynamic limit $\mathcal{A} \rightarrow \infty$:

$$\begin{aligned} \Omega = & -\frac{\mu^2\mathcal{A}}{2g} - \frac{p_{\max}^2\mathcal{A}}{4\pi\beta\hbar^2} + \frac{m\mu\mathcal{A} \log(1 + \frac{p_{\max}^2}{4m\mu})}{2\pi\beta\hbar^2} \\ & - \frac{p_{\max}^2\mathcal{A} \log(\frac{2m}{\beta\sqrt{p_{\max}^4 + 4m\mu p_{\max}^2}})}{4\pi\beta\hbar^2} \end{aligned} \quad (\text{B.14})$$

and

$$\delta N = \frac{m\mathcal{A} \left(\log(1 + \frac{p_{\max}^2}{4m\mu}) + \log(\frac{p_{\max}^2\mathcal{A}}{\hbar^2}) \right)}{4\pi\beta\hbar^2}. \quad (\text{B.15})$$

By using the thermodynamic relations (B.11), we get

$$N = \frac{\mu\mathcal{A}}{g} - \frac{m\mathcal{A} \log(1 + \frac{p_{\max}^2}{4m\mu})}{2\pi\beta\hbar^2} \quad (\text{B.16})$$

and

$$E = \frac{\mu^2\mathcal{A}}{2g} + \frac{p_{\max}^2\mathcal{A}}{4\pi\beta\hbar^2} - \frac{m\mu\mathcal{A} \log(1 + \frac{p_{\max}^2}{4m\mu})}{2\pi\beta\hbar^2}. \quad (\text{B.17})$$

Appendix B.2.

We next determine the chemical potential μ , which fixes the total density $\rho = mN/\mathcal{A}$ at a given value, by solving the equation

$$\rho - \frac{m\mu}{g} + \frac{m^2 \log(1 + \frac{p_{\max}^2}{4m\mu})}{2\pi\beta\hbar^2} = 0; \quad (\text{B.18})$$

at $\beta = \infty$, i.e., zero temperature (subscript 0) we obtain

$$\mu_0 = \frac{g\rho}{m}; \quad (\text{B.19})$$

to order β^{-1} we get

$$\mu = \mu_0 + \delta\mu, \quad (\text{B.20})$$

where

$$\delta\mu = \frac{mg(4g\rho^2 + \rho p_{\max}^2) \log(1 + \frac{p_{\max}^2}{4g\rho})}{m^2 p_{\max}^2 + 2\pi\beta\hbar^2 \rho p_{\max}^2 + 8\pi\beta\hbar^2 g\rho^2}. \quad (\text{B.21})$$

We insert μ from (B.20) into (B.15), define the change in density $\delta\rho = m\delta N/\mathcal{A}$, use the energy E from (B.17), and then expand to order β^{-1} to obtain

$$\delta\rho = \frac{m^2 \left(\log\left(1 + \frac{p_{\max}^2}{4g\rho}\right) + \log\left(\frac{p_{\max}^2 \mathcal{A}}{\hbar^2}\right) \right)}{4\pi\beta\hbar^2} \quad (\text{B.22})$$

and

$$E = \frac{g\rho^2 \mathcal{A}}{2m^2} + \frac{p_{\max}^2 \mathcal{A}}{4\pi\beta\hbar^2}. \quad (\text{B.23})$$

By using (B.4) and $\rho = m |\langle \psi \rangle|^2$, we obtain

$$\tilde{\beta}_{\text{BKT}} = \frac{1}{k_{\text{B}} \tilde{T}_{\text{BKT}}} = \frac{2m^2}{\pi\rho\hbar^2}, \quad (\text{B.24})$$

which we can use along with (B.22) to relate the condensate relative depletion $\delta\rho/\rho$ to $\beta/\tilde{\beta}_{\text{BKT}}$, where $\beta = 1/(k_{\text{B}}T)$ and k_{B} is the Boltzmann constant, as given below:

$$\frac{\delta\rho}{\rho} = \frac{\tilde{\beta}_{\text{BKT}}}{8\beta} \log \left(\frac{p_{\max}^2 \left(1 + \frac{p_{\max}^2}{4g\rho}\right) \mathcal{A}}{\hbar^2} \right). \quad (\text{B.25})$$

We use this low-temperature result (B.25) to estimate the inverse-temperature scale β_{BKT} , at which the depletion of the $k = 0$ condensate mode becomes significant for a finite-size system with N_c^2 collocation points (which fixes the maximum momentum p_{\max}); in particular, we can solve (B.25), for $\delta\rho/\rho = 1$, to obtain

$$\frac{\beta_{\text{BKT}}}{\tilde{\beta}_{\text{BKT}}} = \frac{1}{8} \log \left(\frac{p_{\max}^2 \left(1 + \frac{p_{\max}^2}{4g\rho}\right) \mathcal{A}}{\hbar^2} \right). \quad (\text{B.26})$$

By making the replacements that correspond to defining \hbar , m , and g in terms of c and ξ , as in [51], $p_{\max} \rightarrow \hbar k_{\max}$, $\hbar \rightarrow \sqrt{2}cm\xi$, and $g \rightarrow c^2m^2/\rho$, we can rewrite (B.26) as

$$\frac{\beta_{\text{BKT}}}{\tilde{\beta}_{\text{BKT}}} = \frac{1}{8} \log \left(k_{\max}^2 \mathcal{A} \left(1 + \frac{k_{\max}^2 \xi^2}{2}\right) \right). \quad (\text{B.27})$$

Appendix B.3.

Our DNS runs, which use initial conditions of type IC1 and IC2, give the dynamical evolutions of the Fourier-truncated, 2D GP equation, which is a Hamiltonian system. The energy E , particle number N , and area \mathcal{A} are conserved in this evolution, so our calculation can be viewed as a simulation of this Hamiltonian system in the microcanonical ensemble, which yields, eventually, the fully thermalized state that we have described above. Therefore, we now transform the results, which we have obtained in the previous subsection, into their counterparts in the microcanonical ensemble. In the low-temperature limit, (B.23) yields

$$\beta = \frac{m^2 p_{\max}^2 \mathcal{A}}{2\pi\hbar^2 (2m^2 E - g\rho^2 \mathcal{A})}. \quad (\text{B.28})$$

The energy of a pure condensate is

$$E_0 = \lim_{\beta \rightarrow \infty} E = \frac{g \rho^2 \mathcal{A}}{2 m^2}; \quad (\text{B.29})$$

and the energy and the inverse temperature β (B.28) can be related as follows:

$$E = E_0(1 + \delta\mathcal{E}), \quad (\text{B.30})$$

where $\delta\mathcal{E}$ is the relative increase of energy above E_0 , and

$$\beta = \frac{m^2 p_{\max}^2}{2\pi \hbar^2 g \rho^2 \delta\mathcal{E}}. \quad (\text{B.31})$$

If we now substitute $\beta = \beta_{\text{BKT}}$ by using (B.26), we obtain, in terms of c , ξ and ρ (see text just below (B.26))

$$E_0 = \frac{c^2 \rho \mathcal{A}}{2}, \quad (\text{B.32})$$

$$\delta\tilde{\mathcal{E}}_{\text{BKT}} = \frac{k_{\max}^2 \xi^2}{2}, \quad (\text{B.33})$$

and

$$\delta\mathcal{E}_{\text{BKT}} = \frac{4k_{\max}^2 \xi^2}{\log\left(k_{\max}^2 \mathcal{A} \left(1 + \frac{k_{\max}^2 \xi^2}{2}\right)\right)}. \quad (\text{B.34})$$

All the energies mentioned in the main paper are dimensionless; thus, to convert the energies given in this Appendix to dimensionless forms, we divide them by \hbar . Hence, the energy of a pure condensate is obtained, in the dimensionless form, by dividing (B.29) by \hbar , which gives

$$E_0 = \frac{g}{2\mathcal{A}} = \frac{1}{2} \frac{g}{L^2}. \quad (\text{B.35})$$

References

- [1] R. P. Feynman. Application of quantum mechanics to liquid helium. In C. J. Gorter, editor, *Progress in Low Temperature Physics*, volume I, page 17. North-Holland, Amsterdam, 1955.
- [2] W. F. Vinen. Mutual Friction in a Heat Current in Liquid Helium II. I. Experiments on Steady Heat Currents. *Proceedings of the Royal Society A*, 240(1220):114–127, April 1957.
- [3] W. F. Vinen. Mutual Friction in a Heat Current in Liquid Helium II. II. Experiments on Transient Effects. *Proceedings of the Royal Society A*, 240(1220):128–143, April 1957.
- [4] W. F. Vinen. Mutual Friction in a Heat Current in Liquid Helium II. III. Theory of the Mutual Friction. *Proceedings of the Royal Society A*, 242(1231):493–515, November 1957.
- [5] D. R. Tilley and J. Tilley. *Superfluidity and Superconductivity*. IOP Publishing, Bristol, 3 edition, 1990.
- [6] R.J. Donnelly. *Quantized vortices in helium II*, volume 3. Cambridge University Press, 1991.
- [7] C. F. Barenghi, R. J. Donnelly, and W. F. Vinen, editors. *Quantized Vortex Dynamics and Superfluid Turbulence*, volume 571 of *Lecture Notes in Physics*, Berlin Springer Verlag, 2001.
- [8] W. F. Vinen and J. J. Niemela. Quantum turbulence. *J. Low Temp. Phys.*, 128(5):167–231, 2002.
- [9] J. J. Niemela. Reconnecting to superfluid turbulence. *Physics*, 1:26, Oct 2008.

- [10] I. Procaccia and K. R. Sreenivasan. The state of the art in hydrodynamic turbulence: Past successes and future challenges. *Physica D: Nonlinear Phenomena*, 237(1417):2167 – 2183, 2008. Euler Equations: 250 Years On – Proceedings of an international conference.
- [11] M. Tsubota. Quantum Turbulence. *J. Phys. Soc. Jpn.*, 77(11):111006, 2008.
- [12] M. S. Paoletti and D. P. Lathrop. Quantum turbulence. *Annu. Rev. Condens. Matter Phys.*, 2:213–234, March 2011.
- [13] L. Skrbek and K. R. Sreenivasan. Developed quantum turbulence and its decay. *Phys. Fluids*, 24:011301, 2012.
- [14] J. Maurer and P. Tabeling. Local investigation of superfluid turbulence. *EPL (Europhysics Letters)*, 43(1):29, 1998.
- [15] M. R. Smith, R. J. Donnelly, N. Goldenfeld, and W. F. Vinen. Decay of vorticity in homogeneous turbulence. *Phys. Rev. Lett.*, 71:2583–2586, Oct 1993.
- [16] S. R. Stalp, L. Skrbek, and R. J. Donnelly. Decay of Grid Turbulence in a Finite Channel. *Phys. Rev. Lett.*, 82:4831–4834, Jun 1999.
- [17] L. Skrbek, J. J. Niemela, and R. J. Donnelly. Four Regimes of Decaying Grid Turbulence in a Finite Channel. *Phys. Rev. Lett.*, 85:2973–2976, Oct 2000.
- [18] L. Skrbek and S. R. Stalp. On the decay of homogeneous isotropic turbulence. *Phys. Fluids*, 12(8):1997–2019, 2000.
- [19] S. R. Stalp, J. J. Niemela, W. F. Vinen, and R. J. Donnelly. Dissipation of grid turbulence in helium II. *Phys. Fluids*, 14(4):1377–1379, 2002.
- [20] S. N. Fisher, A. J. Hale, A. M. Guénault, and G. R. Pickett. Generation and Detection of Quantum Turbulence in Superfluid ^3He – B. *Phys. Rev. Lett.*, 86:244–247, Jan 2001.
- [21] E. A. L. Henn, J. A. Seman, G. Roati, K. M. F. Magalhães, and V. S. Bagnato. Emergence of Turbulence in an Oscillating Bose-Einstein Condensate. *Phys. Rev. Lett.*, 103:045301, Jul 2009.
- [22] T. W. Neely, A. S. Bradley, E. C. Samson, S. J. Rooney, E. M. Wright, K. J. H. Law, R. Carretero-Gonzalez, P. G. Kevrekidis, M. J. Davis, and B. P. Anderson. Characteristics of Two-Dimensional Quantum Turbulence in a Compressible Superfluid. *arXiv*, arXiv:1204.1102v2, April 2012.
- [23] C. Sun, S. Jia, C. Barsi, S. Rica, A. Picozzi, and J. W. Fleischer. Observation of the kinetic condensation of classical waves. *Nature Physics*, 8:470474, 2012.
- [24] P.-E. Roche, C. F. Barenghi, and E. Leveque. Quantum turbulence at finite temperature: The two-fluids cascade. *EPL (Europhysics Letters)*, 87(5):54006, 2009.
- [25] J. Salort, P.-E. Roche, and E. Lévêque. Mesoscale equipartition of kinetic energy in quantum turbulence. *EPL (Europhysics Letters)*, 94(2):24001, 2011.
- [26] K. W. Schwarz. Three-dimensional vortex dynamics in superfluid ^4He : Line-line and line-boundary interactions. *Phys. Rev. B*, 31:5782–5804, May 1985.
- [27] K. W. Schwarz. Three-dimensional vortex dynamics in superfluid ^4He : Homogeneous superfluid turbulence. *Phys. Rev. B*, 38:2398–2417, Aug 1988.
- [28] C. F. Barenghi and D. C. Samuels. Self-consistent decay of superfluid turbulence. *Phys. Rev. B*, 60:1252–1260, Jul 1999.
- [29] H. Adachi, S. Fujiyama, and M. Tsubota. Steady-state counterflow quantum turbulence: Simulation of vortex filaments using the full Biot-Savart law. *Phys. Rev. B*, 81:104511, Mar 2010.
- [30] Yu. M. Kagan, B. V. Svistunov, and G. V. Shlyapnikov. Kinetics of Bose condensation in an interacting Bose gas. *Soviet Physics, JETP*, 75(2):387, August 1992.
- [31] V. E. Zakharov and S. V. Nazarenko. Dynamics of the Bose-Einstein condensation. *Physica D*, 201:203–211, 2005.
- [32] B. V. Svistunov. Highly nonequilibrium Bose condensation in a weakly interacting gas. *Journal of the Moscow Physical Society*, 1:373, 1991.
- [33] Yu. Lvov, S. V. Nazarenko, and R. J. West. Wave turbulence in Bose-Einstein condensates. *Physica D*, 184:333 – 351, 2003.
- [34] J. Koplik and H. Levine. Vortex reconnection in superfluid helium. *Phys. Rev. Lett.*, 71:1375–1378,

Aug 1993.

- [35] C. Nore, M. Abid, and M. E. Brachet. Kolmogorov Turbulence in Low-Temperature Superflows. *Phys. Rev. Lett.*, 78:3896–3899, May 1997.
- [36] N. G. Berloff and B. V. Svistunov. Scenario of strongly nonequilibrated Bose-Einstein condensation. *Phys. Rev. A*, 66:013603, Jul 2002.
- [37] M. Kobayashi and M. Tsubota. Kolmogorov Spectrum of Superfluid Turbulence: Numerical Analysis of the Gross-Pitaevskii Equation with a Small-Scale Dissipation. *Phys. Rev. Lett.*, 94:065302, Feb 2005.
- [38] G. Krstulovic and M. Brachet. Dispersive Bottleneck Delaying Thermalization of Turbulent Bose-Einstein Condensates. *Phys. Rev. Lett.*, 106:115303, Mar 2011.
- [39] A. C. White, C. F. Barenghi, N. P. Proukakis, A. J. Youd, and D. H. Wacks. Nonclassical Velocity Statistics in a Turbulent Atomic Bose-Einstein Condensate. *Phys. Rev. Lett.*, 104:075301, Feb 2010.
- [40] C. Connaughton, C. Josserand, A. Picozzi, Y. Pomeau, and S. Rica. Condensation of Classical Nonlinear Waves. *Phys. Rev. Lett.*, 95:263901, Dec 2005.
- [41] S. Nazarenko and M. Onorato. Freely decaying turbulence and Bose-Einstein condensation in Gross-Pitaevskii model. *J. Low Temp Phys.*, 146:31–46, Jan 2007.
- [42] R. Numasato, M. Tsubota, and V. S. L'vov. Direct energy cascade in two-dimensional compressible quantum turbulence. *Phys. Rev. A*, 81:063630, Jun 2010.
- [43] B. Nowak, D. Sexty, and T. Gasenzer. Superfluid turbulence: Nonthermal fixed point in an ultracold Bose gas. *Phys. Rev. B*, 84:020506, Jul 2011.
- [44] A. S. Bradley and B. P. Anderson. Energy Spectra of Vortex Distributions in Two-Dimensional Quantum Turbulence. *Phys. Rev. X*, 2:041001, Oct 2012.
- [45] B. Nowak, J. Schole, D. Sexty, and T. Gasenzer. Nonthermal fixed points, vortex statistics, and superfluid turbulence in an ultracold Bose gas. *Phys. Rev. A*, 85:043627, Apr 2012.
- [46] M. T. Reeves, B. P. Anderson, and A. S. Bradley. Classical and quantum regimes of two-dimensional turbulence in trapped Bose-Einstein condensates. *Phys. Rev. A*, 86:053621, Nov 2012.
- [47] E. Small, R. Pugatch, and Y. Silberberg. Berezinskii-Kosterlitz-Thouless crossover in a photonic lattice. *Phys. Rev. A*, 83:013806, Jan 2011.
- [48] C. Cichowlas, P. Bonaiti, F. Debbasch, and M. Brachet. Effective Dissipation and Turbulence in Spectrally Truncated Euler Flows. *Phys. Rev. Lett.*, 95:264502, Dec 2005.
- [49] U. Frisch, S. Kurien, R. Pandit, W. Pauls, S. S. Ray, A. Wirth, and J.-Z. Zhu. Hyperviscosity, Galerkin Truncation, and Bottlenecks in Turbulence. *Phys. Rev. Lett.*, 101:144501, Sep 2008.
- [50] S. S. Ray, U. Frisch, S. Nazarenko, and T. Matsumoto. Resonance phenomenon for the Galerkin-truncated Burgers and Euler equations. *Phys. Rev. E*, 84:016301, Jul 2011.
- [51] G. Krstulovic and M. Brachet. Energy cascade with small-scale thermalization, counterflow metastability, and anomalous velocity of vortex rings in Fourier-truncated Gross-Pitaevskii equation. *Phys. Rev. E*, 83:066311, Jun 2011.
- [52] J. B. Kogut. An introduction to lattice gauge theory and spin systems. *Rev. Mod. Phys.*, 51:659–713, Oct 1979.
- [53] P. M. Chaikin and T. C. Lubensky. *Principles of Condensed Matter Physics*. Cambridge University Press, Cambridge, 1995.
- [54] C. J. Foster, P. B. Blakie, and M. J. Davis. Vortex pairing in two-dimensional Bose gases. *Phys. Rev. A*, 81:023623, Feb 2010.
- [55] C. J. Pethick and H. Smith. *Bose-Einstein condensation in dilute gases*. Cambridge university press, 2001.
- [56] A. Posazhennikova. Colloquium: Weakly interacting, dilute Bose gases in 2D. *Rev. Mod. Phys.*, 78:1111–1134, Oct 2006.
- [57] N. D. Mermin and H. Wagner. Absence of Ferromagnetism or Antiferromagnetism in One- or Two-Dimensional Isotropic Heisenberg Models. *Phys. Rev. Lett.*, 17:1133–1136, Nov 1966.

- [58] P. C. Hohenberg. Existence of Long-Range Order in One and Two Dimensions. *Phys. Rev.*, 158:383–386, June 1967.
- [59] V. L. Berezinskii. Destruction of Long-range Order in One-dimensional and Two-dimensional Systems having a Continuous Symmetry Group I. Classical Systems. *Soviet Physics, JETP*, 32(3):493, March 1971.
- [60] J. M. Kosterlitz and D. J. Thouless. Ordering, metastability and phase transitions in two-dimensional systems. *Journal of Physics C: Solid State Physics*, 6(7):1181, 1973.
- [61] <http://www.fft.w.org>.
- [62] R. Kubo. The fluctuation-dissipation theorem. *Reports on Progress in Physics*, 29(1):255, 1966.
- [63] M. Miguel and R. Toral. Stochastic Effects in Physical Systems. In Enrique Tirapegui, Javier Martinez, and Rolando Tiemann, editors, *Instabilities and Nonequilibrium Structures VI*, volume 5 of *Nonlinear Phenomena and Complex Systems*, pages 35–127. Springer Netherlands, 2000.
- [64] M. S. Paoletti, M. E. Fisher, K. R. Sreenivasan, and D. P. Lathrop. Velocity Statistics Distinguish Quantum Turbulence from Classical Turbulence. *Phys. Rev. Lett.*, 101:154501, Oct 2008.
- [65] H. Adachi and M. Tsubota. Numerical study of velocity statistics in steady counterflow quantum turbulence. *Phys. Rev. B*, 83:132503, Apr 2011.
- [66] P. Davide, S. Nazarenko, and M. Onorato. Sustained turbulence in the three-dimensional GrossPitaevskii model. *Physica D: Nonlinear Phenomena*, 241(3):304 – 314, 2012. Special Issue on Small Scale Turbulence.
- [67] G. Düring, A. Picozzi, and S. Rica. Breakdown of weak-turbulence and nonlinear wave condensation. *Physica D: Nonlinear Phenomena*, 238(16):1524 – 1549, 2009.
- [68] K. Damle, S. N. Majumdar, and S. Sachdev. Phase ordering kinetics of the Bose gas. *Phys. Rev. A*, 54:5037–5041, Dec 1996.
- [69] S. Nazarenko and M. Onorato. Wave turbulence and vortices in BoseEinstein condensation. *Physica D: Nonlinear Phenomena*, 219(1):1 – 12, 2006.
- [70] T. R. Matthew, T. P. Billam, B. P. Anderson, and A. S. Bradley. Inverse Energy Cascade in Forced 2D Quantum Turbulence. *arXiv*, arXiv:1209.5824v1, September 2012.